Additive Manufacturing 76 (2023) 103771

Contents lists available at ScienceDirect

Additive Manufacturing

journal homepage: www.elsevier.com/locate/addma

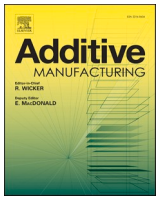

Predicting solid-state phase transformations during metal additive manufacturing: A case study on electron-beam powder bed fusion of Inconel-738

Nana Kwabena Adomako [a], Nima Haghdadi [a,*], James F.L. Dingle [b,c], Ernst Kozeschnik [d], Xiaozhou Liao [b,c], Simon P. Ringer [b,c], Sophie Primig [a,*]

[a] School of Materials Science & Engineering, UNSW Sydney, Kensington, NSW 2052, Australia
[b] Australian Centre for Microscopy & Microanalysis, The University of Sydney, Sydney, NSW 2006, Australia
[c] School of Aerospace, Mechanical & Mechatronic Engineering, The University of Sydney, Sydney, NSW 2006, Australia
[d] Institute for Materials Science and Technology, TU Wien, 1060 Vienna, Austria

ARTICLE INFO

Keywords:
Additive manufacturing
Simulation
Thermal cycles
γ' phase
IN738

ABSTRACT

Metal additive manufacturing (AM) has now become the perhaps most desirable technique for producing complex shaped engineering parts. However, to truly take advantage of its capabilities, advanced control of AM microstructures and properties is required, and this is often enabled via modeling. The current work presents a computational modeling approach to studying the solid-state phase transformation kinetics and the microstructural evolution during AM. Our approach combines thermal and thermo-kinetic modelling. A semi-analytical heat transfer model is employed to simulate the thermal history throughout AM builds. Thermal profiles of individual layers are then used as input for the MatCalc thermo-kinetic software. The microstructural evolution (e.g., fractions, morphology, and composition of individual phases) for any region of interest throughout the build is predicted by MatCalc. The simulation is applied to an IN738 part produced by electron beam powder bed fusion to provide insights into how γ' precipitates evolve during thermal cycling. Our simulations show qualitative agreement with our experimental results in predicting the size distribution of γ' along the build height, its multimodal size character, as well as the volume fraction of MC carbides. Our findings indicate that our method is suitable for a range of AM processes and alloys, to predict and engineer their microstructures and properties.

1. Introduction

Additive manufacturing (AM) is an advanced manufacturing method that enables engineering parts with intricate shapes to be fabricated with high efficiency and minimal materials waste. AM involves building up 3D components layer-by-layer from feedstocks such as powder [1]. Various alloys, including steel, Ti, Al, and Ni-based superalloys, have been produced using different AM techniques. These techniques include directed energy deposition (DED), electron- and laser powder bed fusion (E-PBF and L-PBF), and have found applications in a variety of industries such as aerospace and power generation [2–4]. Despite the growing interest, certain challenges limit broader applications of AM fabricated components in these industries and others. One of such limitations is obtaining a suitable and reproducible microstructure that offers the desired mechanical properties consistently. In fact, the AM as-built microstructure is highly complex and considerably distinctive from its conventionally processed counterparts owing to the complicated thermal cycles arising from the deposition of several layers upon each other [5,6].

Several studies have reported that the solid-state phases and solidification microstructure of AM processed alloys such as CMSX-4, CoCr [7,8], Ti-6Al-4V [9–11], IN738 [6], 304L stainless steel [12], and IN718 [13,14] exhibit considerable variations along the build direction. For instance, references [9,10] have reported that there is a variation in the distribution of α and β phases along the build direction in Ti-alloys. Similarly, the microstructure of an L-PBF fabricated martensitic steel exhibits variations in the fraction of martensite [15]. Furthermore, some of the present authors and others [6,16–20] have recently reviewed and

* Corresponding authors.
E-mail addresses: nima.haghdadi@unsw.edu.au (N. Haghdadi), s.primig@unsw.edu.au (S. Primig).

https://doi.org/10.1016/j.addma.2023.103771
Received 2 March 2023; Received in revised form 29 August 2023; Accepted 3 September 2023
Available online 8 September 2023

reported that there is a difference in the morphology and fraction of nanoscale precipitates as a function of build height in Ni-based superalloys. These non-uniformities in the as-built microstructure result in an undesired heterogeneity in mechanical and other important properties such as corrosion and oxidation [19,21–23]. To obtain the desired microstructure and properties, additional processing treatments are utilized, but this incurs extra costs and may lead to precipitation of detrimental phases and grain coarsening. Therefore, a through-process understanding of the microstructure evolution under repeated heating and cooling is now needed to further advance 3D printed microstructure and property control.

It is now commonly understood that the microstructure evolution during printing is complex, and most AM studies concentrate on the microstructure and mechanical properties of the final build only. Post-printing studies of microstructure characteristics at room temperature miss crucial information on how they evolve. In-situ measurements and modelling approaches are required to better understand the complex microstructural evolution under repeated heating and cooling. Most in-situ measurements in AM focus on monitoring the microstructural changes, such as phase transformations and melt pool dynamics during fabrication using X-ray scattering and high-speed X-ray imaging [24–27]. For example, Zhao et al. [25] measured the rate of solidification and described the α/β phase transformation during L-PBF of Ti-6Al-4V in-situ. Also, Wahlmann et al. [21] recently used an L-PBF machine coupled with X-ray scattering to investigate the changes in CMSX-4 phase during successive melting processes. Although these techniques provide significant understanding of the basic principles of AM, they are not widely accessible. This is due to the great cost of the instrument, competitive application process, and complexities in terms of the experimental set-up, data collection, and analysis [26,28].

Computational modeling techniques are promising and more widely accessible tools that enable advanced understanding, prediction, and engineering of microstructures and properties during AM. So far, the majority of computational studies have concentrated on physics based process models for metal AM, with the goal of predicting the temperature profile, heat transfer, powder dynamics, and defect formation (e.g., porosity) [29,30]. In recent times, there have been efforts in modeling of the AM microstructure evolution using approaches such as phase-field [31], Monte Carlo (MC) [32], and cellular automata (CA) [33], coupled with finite element simulations for temperature profiles. However, these techniques are often restricted to simulating the evolution of solidification microstructures (e.g., grain and dendrite structure) and defects (e.g., porosity). For example, Zinovieva et al. [33] predicted the grain structure of L-PBF Ti-6Al-4V using finite difference and cellular automata methods. However, studies on the computational modelling of the solid-state phase transformations, which largely determine the resulting properties, remain limited. This can be attributed to the multi-component and multi-phase nature of most engineering alloys in AM, along with the complex transformation kinetics during thermal cycling. This kind of research involves predictions of the thermal cycle in AM builds, and connecting it to essential thermodynamic and kinetic data as inputs for the model. Based on the information provided, the thermokinetic model predicts the history of solid-state phase microstructure evolution during deposition as output. For example, a multi-phase, multi-component mean-field model has been developed to simulate the intermetallic precipitation kinetics in IN718 [34] and IN625 [35] during AM. Also, Basoalto et al. [36] employed a computational framework to examine the contrasting distributions of process-induced microvoids and precipitates in two Ni-based superalloys, namely IN718 and CM247LC. Furthermore, McNamara et al. [37] established a computational model based on the Johnson-Mehl-Avrami model for non-isothermal conditions to predict solid-state phase transformation kinetics in L-PBF IN718 and DED Ti-6Al-4V. These models successfully predicted the size and volume fraction of individual phases and captured the repeated nucleation and dissolution of precipitates that occur during AM.

In the current study, we propose a modeling approach with appreciably short computational time to investigate the detailed microstructural evolution during metal AM. This may include obtaining more detailed information on the morphologies of phases, such as size distribution, phase fraction, dissolution and nucleation kinetics, as well as chemistry during thermal cycling and final cooling to room temperature. We utilize the combination of the MatCalc thermo-kinetic simulator and a semi-analytical heat conduction model. MatCalc is a software suite for simulation of phase transformations, microstructure evolution and certain mechanical properties in engineering alloys. It has successfully been employed to simulate solid-state phase transformations in Ni-based superalloys [38,39], steels [40], and Al alloys [41] during complex thermo-mechanical processes. MatCalc uses the classical nucleation theory as well as the so-called Svoboda-Fischer-Fratzl-Kozeschnik (SFFK) growth model as the basis for simulating precipitation kinetics [42]. Although MatCalc was originally developed for conventional thermo-mechanical processes, we will show that it is also applicable for AM if the detailed time-temperature profile of the AM build is known. The semi-analytical heat transfer code developed by Stump and Plotkowski [43] is used to simulate these profile throughout the AM build.

1.1. Application to IN738

Inconel-738 (IN738) is a precipitation hardening Ni-based superalloy mainly employed in high-temperature components, e.g. in gas turbines and aero-engines owing to its exceptional mechanical properties at temperatures up to 980 °C, coupled with high resistance to oxidation and corrosion [44]. Its superior high-temperature strength (~1090 MPa tensile strength) is provided by the $L1_2$ ordered $Ni_3(Al,Ti)$ γ' phase that precipitates in a face-centered cubic (FCC) γ matrix [45,46]. Despite offering great properties, IN738, like most superalloys with high γ' fractions, is challenging to process owing to its propensity to hot cracking [47,48]. Further, machining of such alloys is challenging because of their high strength and work-hardening rates. It is therefore difficult to fabricate complex INC738 parts using traditional manufacturing techniques like casting, welding, and forging.

The emergence of AM has now made it possible to fabricate such parts from IN738 and other superalloys. Some of the current authors' recent research successfully applied E-PBF to fabricate defect-free IN738 containing γ' throughout the build [16,17]. The precipitated γ' were heterogeneously distributed. In particular, Haghdadi et al. [16] studied the origin of the multimodal size distribution of γ', while Lim et al. [17] investigated the gradient in γ' character with build height and its correlation to mechanical properties. Based on these results, the present study aims to extend the understanding of the complex and site-specific microstructural evolution in E-PBF IN738 by using a computational modelling approach. New experimental evidence (e.g., micrographs not published previously) is presented here to support the computational results.

2. Materials and Methods

2.1. Materials preparation

IN738 Ni-based superalloy (59.61Ni-8.48Co-7.00Al-17.47Cr-3.96Ti-1.01Mo-0.81W-0.56Ta-0.49Nb-0.47C-0.09Zr-0.05B, at%) gas-atomized powder was used as feedstock. The powders, with average size of 60 ± 7 μm, were manufactured by Praxair and distributed by Astro Alloys Inc. An Arcam Q10 machine by GE Additive with an acceleration voltage of 60 kV was used to fabricate a 15 × 15 × 25 mm^3 block (XYZ, Z: build direction) on a 316 stainless steel substrate. The block was 3D-printed using a 'random' spot melt pattern. The random spot melt pattern involves randomly selecting points in any given layer, with an equal chance of each point being melted. Each spot melt experienced a dwell time of 0.3 ms, and the layer thickness was 50 μm. Some of the current authors have previously characterized the microstructure of the very

same and similar builds in more detail [16,17]. A preheat temperature of ~1000 °C was set and kept during printing to reduce temperature gradients and, in turn, thermal stresses [49–51]. Following printing, the build was separated from the substrate through electrical discharge machining. It should be noted that this sample was simultaneously printed with the one used in [17] during the same build process and on the same build plate, under identical conditions.

2.2. Microstructural characterization

The printed sample was longitudinally cut in the direction of the build using a Struers Accutom-50, ground, and then polished to 0.25 μm suspension via standard techniques. The polished x-z surface was electropolished and etched using Struers A2 solution (perchloric acid in ethanol). Specimens for image analysis were polished using a 0.06 μm colloidal silica. Microstructure analyses were carried out across the height of the build using optical microscopy (OM) and scanning electron microscopy (SEM) with focus on the microstructure evolution (γ' precipitates) in individual layers. The position of each layer being analyzed was determined by multiplying the layer number by the layer thickness (50 μm). It should be noted that the position of the first layer starts where the thermal profile is tracked (in this case, 2 mm from the bottom). SEM images were acquired using a JEOL 7001 field emission microscope. The brightness and contrast settings, acceleration voltage of 15 kV, working distance of 10 mm, and other SEM imaging parameters were all held constant for analysis of the entire build. The ImageJ software was used for automated image analysis to determine the phase fraction and size of γ' precipitates and carbides. A 2-pixel radius Gaussian blur, following a greyscale thresholding and watershed segmentation was used [52]. Primary γ' sizes (>50 nm), were measured using equivalent spherical diameters. The phase fractions were considered equal to the measured area fraction. Secondary γ' particles (<50 nm) were not considered here. The γ' size in the following refers to the diameter of a precipitate.

2.3. Hardness testing

A Struers DuraScan tester was utilized for Vickers hardness mapping on a polished x-z surface, from top to bottom under a maximum load of 100 mN and 10 s dwell time. 30 micro-indentations were performed per row. According to the ASTM standard [53], the indentations were sufficiently distant (~500 μm) to assure that strain-hardened areas did not interfere with one another.

2.4. Computational simulation of E-PBF IN738 build

2.4.1. Thermal profile modeling

The thermal history was generated using the semi-analytical heat transfer code (also known as the 3DThesis code) developed by Stump and Plotkowski [43]. This code is an open-source C++ program which provides a way to quickly simulate the conductive heat transfer found in welding and AM. The key use case for the code is the simulation of larger domains than is practicable with Computational Fluid Dynamics/Finite Element Analysis programs like FLOW-3D AM. Although simulating conductive heat transfer will not be an appropriate simplification for some investigations (for example the modelling of keyholding or pore formation), the 3DThesis code does provide fast estimates of temperature, thermal gradient, and solidification rate which can be useful for elucidating microstructure formation across entire layers of an AM build. The mathematics involved in the code is as follows:

In transient thermal conduction during welding and AM, with uniform and constant thermophysical properties and without considering fluid convection and latent heat effects, energy conservation can be expressed as:

$$\rho c \frac{\partial T}{\partial t} = k\nabla^2 T + \dot{Q} \tag{1}$$

where ρ is density, c specific heat, T temperature, t time, k thermal conductivity, and $\dot{Q}$ a volumetric heat source. By assuming a semi-infinite domain, Eq. 1 can be analytically solved. The solution for temperature at a given time (t) using a volumetric Gaussian heat source is presented as:

$$T(x,y,z,t) - T_0 = \frac{3\sqrt{3}\eta Q}{\rho c \pi^{\frac{3}{2}}} \int_0^t \frac{1}{\sqrt{\phi_x \phi_y \phi_z}} \exp\left(-3\left(\frac{x'(t')^2}{\phi_x} + \frac{y'(t')^2}{\phi_y} + \frac{z'(t')^2}{\phi_z} \right) \right) dt' \tag{2}$$

$$\text{and } \phi_i = 12\alpha(t - t') + \sigma_i^2 \text{for} i = x,y,z \tag{3}$$

$$\text{and } \boldsymbol{x}'(t') = \boldsymbol{x} - \boldsymbol{x_b}(t') \tag{4}$$

Where $\boldsymbol{x}$ is the vector $\langle x,y,z \rangle$ and $\boldsymbol{x_b}$ is the location of the heat source.

The numerical integration scheme used is an adaptive Gaussian quadrature method based on the following nondimensionalization:

$$s = \frac{\alpha}{\sigma_{xy}^2} t,\ s' = \frac{\alpha}{\sigma_{xy}^2} t',\ X = \frac{x}{\sigma_{xy}},\ Y = \frac{y}{\sigma_{xy}},\ Z = \frac{z}{\sigma_{xy}},\ \delta = \frac{\sigma_z}{\sigma_{xy}} \tag{5}$$

A more detailed explanation of the mathematics can be found in reference [43].

The main source of the thermal cycling present within a powder-bed fusion process is the fusion of subsequent layers. Therefore, regions near the top of a build are expected to undergo fewer thermal cycles than those closer to the bottom. For this purpose, data from the single scan's thermal influence on multiple layers was spliced to represent the thermal cycles experienced at a single location caused by multiple subsequent layers being fused.

The cross-sectional area simulated by this model was kept constant at 1×1 mm^2, and the depth was dependent on the build location modelled with MatCalc. For a build location 2 mm from the bottom, the maximum number of layers to simulate is 460. Fig. 1a shows a stitched overview OM image of the entire build indicating the region where this thermal cycle is simulated and tracked. To increase similarity with the conditions of the physical build, each thermal history was constructed from the results of two simulations generated with different versions of a random scan path. The parameters used for these thermal simulations can be found in Table 1. It should be noted that the main purpose of the thermal profile modelling was to demonstrate how the conditions at different locations of the build change relative to each other. Accurately predicting the absolute temperature during the build would require validation via a temperature sensor measurement during the build process which is beyond the scope of the study. Nonetheless, to establish the viability of the heat source as a suitable approximation for this study, an additional sensitivity analysis was conducted. This analysis focused on the influence of energy input on γ' precipitation behavior, the central aim of this paper. This was achieved by employing varying beam absorption energies (0.76, 0.82 - the values utilized in the simulation, and 0.9). The direct impact of beam absorption efficiency on energy input into the material was investigated. Specifically, the initial 20 layers of the build were simulated and subsequently compared to experimental data derived from SEM. While phase fractions were found to be consistent across all conditions, disparities emerged in the mean size of γ' precipitates. An absorption efficiency of 0.76 yielded a mean size of approximately 70 nm. Conversely, absorption efficiencies of 0.82 and 0.9 exhibited remarkably similar mean sizes of around 130 nm, aligning closely with the outcomes of the experiments.

2.4.2. Thermo-kinetic simulation

The numerical analyses of the evolution of precipitates was

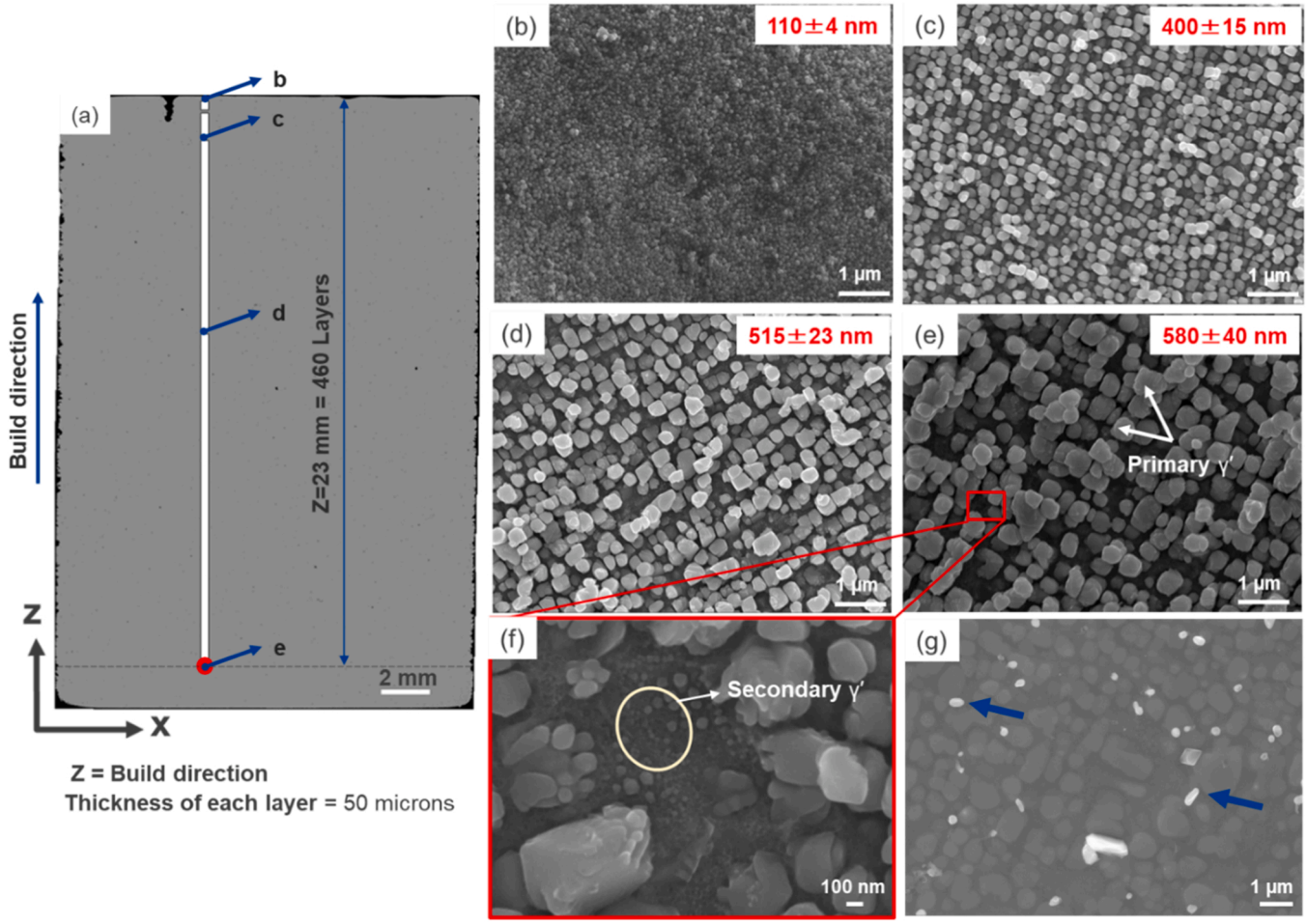

Fig. 1. (a) Stitched overview OM image of the cross-section (X-Z) of the entire crack-free build. The red point represents the region where a thermal cycle was simulated. Z is the build direction, and the height is measured from the simulated region to the top. (b-e) SEM micrographs showing γ' size evolution along X-Z cross-section of (a). (f) and (g) SEM micrographs showing secondary γ' and carbides, respectively. The carbides are observed at the bottom of the build. Arrows in (g) show examples of carbides.

Table 1
A list of parameters used in thermal simulation of E-PBF.

Parameter	Value
Spatial resolution	5 μm
Time step	0.5 s
Beam diameter	200 μm
Beam penetration depth	1 μm
Beam power	1200 W
Beam absorption efficiency	0.82
Thermal conductivity	25.37 W/(m·K)
Chamber temperature	1000 °C
Specific heat	711.756 J/(kg·K)
Density	8110 kg/m^3

performed using MatCalc version 6.04 (rel 0.011). The thermodynamic ('mc_ni.tdb', version 2.034) and diffusion ('mc_ni.ddb', version 2.007) databases were used. MatCalc's basic principles are elaborated as follows:

The nucleation kinetics of precipitates are computed using a computational technique based on a classical nucleation theory [54] that has been modified for systems with multiple components [42,55]. Accordingly, the transient nucleation rate (J), which expresses the rate at which nuclei are formed per unit volume and time, is calculated as:

$$J = N_0 Z \beta^* \bullet exp\left(\frac{-G^*}{k \bullet T}\right) \bullet \exp\left(\frac{-\tau}{t}\right) \tag{6}$$

where N_0 denotes the number of active nucleation sites, β^* the rate of atomic attachment, k the Boltzmann constant, T the temperature, G^* the critical energy for nucleus formation, τ the incubation time, and t the time. Z (Zeldovich factor) takes into consideration that thermal excitation destabilizes the nucleus as opposed to its inactive state [54]. Z is defined as follows:

$$z = \left[\frac{-1}{2\pi kT} \left.\frac{\partial^2 \Delta G}{\partial n^2}\right|_{n*}\right]^{\frac{1}{2}} \tag{7}$$

where ΔG is the overall change in free energy due to the formation of a nucleus and n is the nucleus' number of atoms. ΔG's derivative is evaluated at n^* (critical nucleus size). β^* accounts for the long-range diffusion of atoms required for nucleation, provided that the matrix' and precipitates' composition differ. Svoboda et al. [42] developed an appropriate multi-component equation for β^*, which is given by:

$$\beta^* = \frac{4\pi\rho^{*2}}{a^4 \Omega} \left[\sum_{i=1}^{n} \frac{(c_{ki} - c_{0i})^2}{c_{0i} D_{0i}}\right]^{-1} \tag{8}$$

where ρ^* denotes the critical radius for nucleation, a represents atomic distance, and Ω is the molar volume. c_{ki} and c_{0i} represent the concentration of elements in the precipitate and matrix, respectively. The parameter D_{0i} denotes the rate of diffusion of the i^{th} element within the matrix. The expression for the incubation time τ is expressed as [54]:

$$\tau = \frac{1}{2\beta^* Z^2} \tag{9}$$

and G^*, which represents the critical energy for nucleation:

$$G^* = \frac{16\pi}{3}\frac{\gamma^3}{(\Delta G_{vol})^2} \tag{10}$$

where γ is the interfacial energy, and ΔG_{vol} the change in the volume free energy. The critical nucleus' composition is similar to the γ' phase's equilibrium composition at the same temperature. γ is computed based on the precipitate and matrix compositions, using a generalized nearest neighbor broken bond model, with the assumption of interfaces being planar, sharp, and coherent [56–58].

In Eq. 7, it is worth noting that G^* represents the fundamental variable in the nucleation theory. It contains $\gamma^3/(\Delta G_{vol})^2$ and is in the exponent of the nucleation rate. Therefore, even small variations in γ and/or ΔG_{vol} can result in notable changes in J, especially if G^* is in the order of $k \bullet T$. This is demonstrated in [38] for UDIMET 720 Li during continuous cooling, where these quantities change steadily during precipitation due to their dependence on matrix' and precipitate's temperature and composition. In the current work, these changes will be even more significant as the system is exposed to multiple cycles of rapid cooling and heating.

Once nucleated, the growth of a precipitate is assessed using the radius and composition evolution equations developed by Svoboda et al. [42] with a mean-field method that employs the thermodynamic extremal principle. The expression for the total Gibbs free energy of a thermodynamic system G, which consists of n components and m precipitates, is given as follows:

$$G = \sum_{i}^{n} N_{0i}\mu_{0i} + \sum_{k=1}^{m}\frac{4\pi\rho_k^3}{3}\left(\lambda_k + \sum_{i=1}^{n} c_{ki}\mu_{ki}\right) + \sum_{k=1}^{m} 4\pi{\rho_k}^2\gamma_k. \tag{11}$$

The chemical potential of component i in the matrix is denoted as $\mu_{0i}(i = 1, \ldots, n)$, while the chemical potential of component i in the precipitate is represented by $\mu_{ki}(k = 1,\ldots,m,i = 1,\ldots,n)$. These chemical potentials are defined as functions of the concentrations $\mu_{ki}(k = 1,\ldots,m,i = 1, \ldots, n)$. The interface energy density is denoted as γ, and λ_k incorporates the effects of elastic energy and plastic work resulting from the volume change of each precipitate.

Eq. (12) establishes that the total free energy of the system in its current state relies on the independent state variables: the sizes (radii) of the precipitates ρ_k and the concentrations of each component c_{ki}. The remaining variables can be determined by applying the law of mass conservation to each component i. This can be represented by the equation:

$$N_i = N_{0i} + \sum_{k=1}^{m}\frac{4\pi\rho_k^3}{3}c_{ki}, \tag{12}$$

Furthermore, the global mass conservation can be expressed by equation:

$$N = \sum_{i=1}^{n} N_i \tag{13}$$

When a thermodynamic system transitions to a more stable state, the energy difference between the initial and final stages is dissipated. This model considers three distinct forms of dissipation effects [42]. These include dissipations caused by the movement of interfaces, diffusion within the precipitate and diffusion within the matrix.

Consequently, $\dot{\rho}_k$ (growth rate) and $\dot{c}_{ki}$ (chemical composition's rate of change) of the precipitate with index k are derived from the linear system of equation system:

$$A_{ij}y_j = B_i \tag{14}$$

where y_j symbolizes the rates $\dot{\rho}_k$ and $\dot{c}_{ki}$ [42]. Index i contains variables for precipitate radius, chemical composition, and stoichiometric boundary conditions suggested by the precipitate's crystal structure. Eq. (10) is computed separately for every precipitate k. For a more detailed description of the formulae for the coefficients A_{ij} and B_i employed in this work please refer to [59].

The MatCalc software was used to perform the numerical time integration of $\dot{\rho}_k$ and $\dot{c}_{ki}$ of precipitates based on the classical numerical method by Kampmann and Wagner [60]. Detailed information on this method can be found in [61]. Using this computational method, calculations for E-PBF thermal cycles (cyclic heating and cooling) were computed and compared to experimental data. The simulation took approximately 2–4 hrs to complete on a standard laptop.

3. Results

3.1. Microstructure

Fig. 1 displays a stitched overview image and selected SEM micrographs of various γ' morphologies and carbides after observations of the X-Z surface of the build from the top to 2 mm above the bottom. Fig. 2 depicts a graph that charts the average size and phase fraction of the primary γ', as it changes with distance from the top to the bottom of the build. The SEM micrographs show widespread primary γ' precipitation throughout the entire build, with the size increasing in the top to bottom direction. Particularly, at the topmost height, representing the 460th layer (Z = 22.95 mm), as seen in Fig. 1b, the average size of γ' is 110 ± 4 nm, exhibiting spherical shapes. This is representative of the

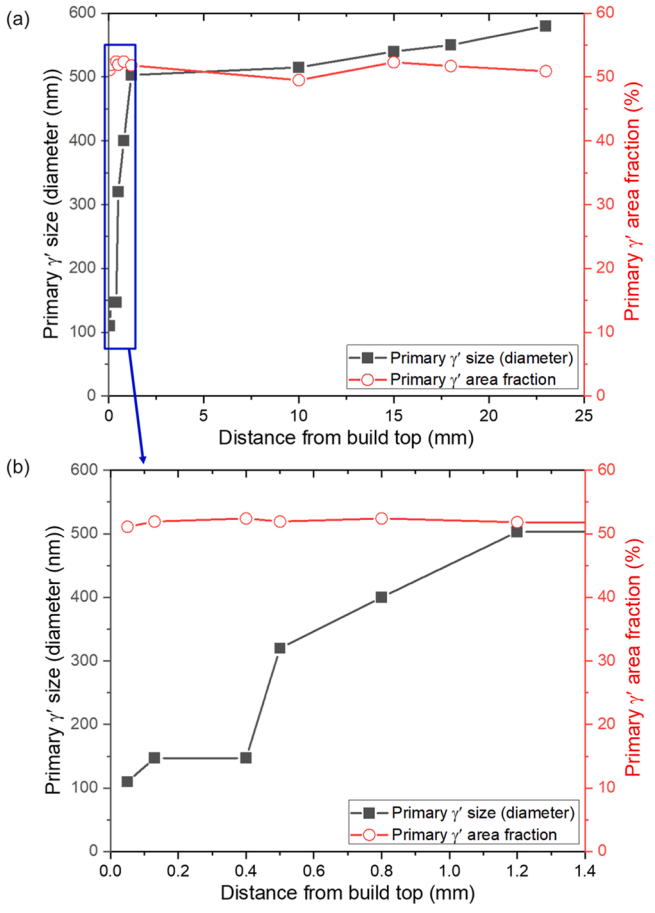

Fig. 2. (a) Average size and fraction of primary γ' versus distance from the top of the build towards the bottom. (b) is a magnified view of the first few layers in (a).

microstructure after it solidifies and cools to room temperature, without experiencing additional thermal cycles. The γ′ size slightly increases to 147 ± 6 nm below this layer and remains constant until 0.4 mm (~453rd layer) from the top. At this position, the microstructure still closely resembles that of the 460th layer. After the 453rd layer, the γ′ size grows rapidly to ~503 ± 19 nm until reaching the 437th layer (1.2 mm from top). The γ′ particles here have a cuboidal shape, and a small fraction is coarser than 600 nm. γ′ continue to grow steadily from this position to the bottom (23 mm from the top). A small fraction of γ′ is > 800 nm.

Besides primary γ′, secondary γ′ with sizes ranging from 5 to 50 nm were also found. These secondary γ′ precipitates, as seen in Fig. 1f, were present only in the bottom and middle regions. A detailed analysis of the multimodal size distribution of γ′ can be found in [16]. There is no significant variation in the phase fraction of the γ′ along the build. The phase fraction is ~ 52%, as displayed in Fig. 2. It is worth mentioning that the total phase fraction of γ′ was estimated based on the primary γ′ phase fraction because of the small size of secondary γ′. Spherical MC carbides with sizes ranging from 50 to 400 nm and a phase fraction of 0.8% were also observed throughout the build. The carbides are the light grey precipitates in Fig. 1g. The light grey shade of carbides in the SEM images is due to their composition and crystal structure [52]. These carbides are not visible in Fig. 1b-e because they were dissolved during electro-etching carried out after electropolishing. In Fig. 1g, however, the sample was examined directly after electropolishing, without electro-etching.

Table 2 shows the nominal and measured composition of γ′ precipitates throughout the build by atom probe microscopy as determined in our previous study [17]. No build height-dependent composition difference was observed in either of the γ′ precipitate populations. However, there was a slight disparity between the composition of primary and secondary γ′. Among the main γ′ forming elements, the primary γ′ has a high Ti concentration while secondary γ′ has a high Al concentration. A detailed description of the atom distribution maps and the proxigrams of the constituent elements of γ′ throughout the build can be found in [17].

3.2. Hardness

Fig. 3a shows the Vickers hardness mapping performed along the entire X-Z surface, while Fig. 3b shows the plot of average hardness at different build heights. This hardness distribution is consistent with the γ′ precipitate size gradient across the build direction in Figs. 1 and 2. The maximum hardness of ~530 HV1 is found at ~0.5 mm away from the top surface (Z = 22.5), where γ′ particles exhibit the smallest observed size in Fig. 2b. Further down the build (~ 2 mm from the top), the hardness drops to the 440–490 HV1 range. This represents the region where γ′ begins to coarsen. The hardness drops further to 380–430 HV1 at the bottom of the build.

3.3. Modeling of the microstructural evolution during E-PBF

3.3.1. Thermal profile modeling

Fig. 4 shows the simulated thermal profile of the E-PBF build at a location of 23 mm from the top of the build, using a semi-analytical heat conduction model. This profile consists of the time taken to deposit 460 layers until final cooling, as shown in Fig. 4a. Fig. 4b-d show the magnified regions of Fig. 4a and reveal the first 20 layers from the top, a single layer (first layer from the top), and the time taken for the build to cool after the last layer deposition, respectively.

The peak temperatures experienced by previous layers decrease progressively as the number of layers increases but never fall below the build preheat temperature (1000 °C). Our simulated thermal cycle may not completely capture the complexity of the actual thermal cycle utilized in the E-PBF build. For instance, the top layer (Fig. 4c), also representing the first deposit's thermal profile without additional cycles (from powder heating, melting, to solidification), recorded the highest peak temperature of 1390 °C. Although this temperature is above the melting range of the alloy (1230–1360 °C) [62], we believe a much higher temperature was produced by the electron beam to melt the powder. Nevertheless, the solidification temperature and dynamics are outside the scope of this study as our focus is on the solid-state phase transformations during deposition. It takes ~25 s for each layer to be deposited and cooled to the build temperature. The interlayer dwell time is 125 s. The time taken for the build to cool to room temperature (RT) after final layer deposition is ~4.7 hrs (17,000 s).

3.3.2. MatCalc simulation

During the MatCalc simulation, the matrix phase is defined as γ. γ′, and MC carbide are included as possible precipitates. The domain of these precipitates is set to be the matrix (γ), and nucleation is assumed to be homogenous. In homogeneous nucleation, all atoms of the unit volume are assumed to be potential nucleation sites. Table 3 shows the computational parameters used in the simulation. All other parameters were set at default values as recommended in the version 6.04.0011 of MatCalc. The values for the interfacial energies are automatically calculated according to the generalized nearest neighbor broken bond model and is one of the most outstanding features in MatCalc [56–58]. It should be noted that the elastic misfit strain was not included in the calculation. The output of MatCalc includes phase fraction, size, nucleation rate, and composition of the precipitates. The phase fraction in MatCalc is the volume fraction. Although the experimental phase fraction is the measured area fraction, it is relatively similar to the volume fraction. This is because of the generally larger precipitate size and similar morphology at the various locations along the build [63]. A reliable phase fraction comparison between experiment and simulation can therefore be made.

3.3.2.1. Precipitate phase fraction. Fig. 5a shows the simulated phase fraction of γ′ and MC carbide during thermal cycling. Fig. 5b is a

Table 2
Bulk IN738 composition determined using inductively coupled plasma atomic emission spectroscopy (ICP-AES). Compositions of γ, primary γ′, and secondary γ′ at various locations in the build measured by APT. This information is reproduced from data in Ref. [17] with permission.

at%	Ni	Cr	Co	Al	Mo	W	Ti	Nb	C	B	Zr	Ta	Others
Bulk	59.12	17.47	8.48	7.00	1.01	0.81	3.96	0.49	0.47	0.05	0.09	0.56	0.46
γ matrix													
Top	50.48	32.91	11.59	1.94	1.39	0.82	0.44	0.8	0.03	0.03	0.02	-	0.24
Mid	50.37	32.61	11.93	1.79	1.54	0.89	0.44	0.1	0.03	0.02	0.02	0.01	0.23
Bot	48.10	34.57	12.08	2.14	1.43	0.88	0.48	0.08	0.04	0.03	0.01	-	0.12
Primary γ′													
Top	72.17	2.51	3.44	12.71	0.25	0.39	7.78	0.56	-	0.03	0.02	0.05	0.08
Mid	71.60	2.57	3.28	13.55	0.42	0.68	7.04	0.73	-	0.01	0.03	0.04	0.04
Bot	72.34	2.47	3.86	12.50	0.26	0.44	7.46	0.50	0.05	0.02	0.02	0.03	0.04
Secondary γ′													
Mid	70.42	4.20	3.23	14.19	0.63	1.03	5.34	0.79	0.03	-	0.04	0.04	0.05
Bot	69.91	4.06	3.68	14.32	0.81	1.04	5.22	0.65	0.05	-	0.10	0.02	0.11

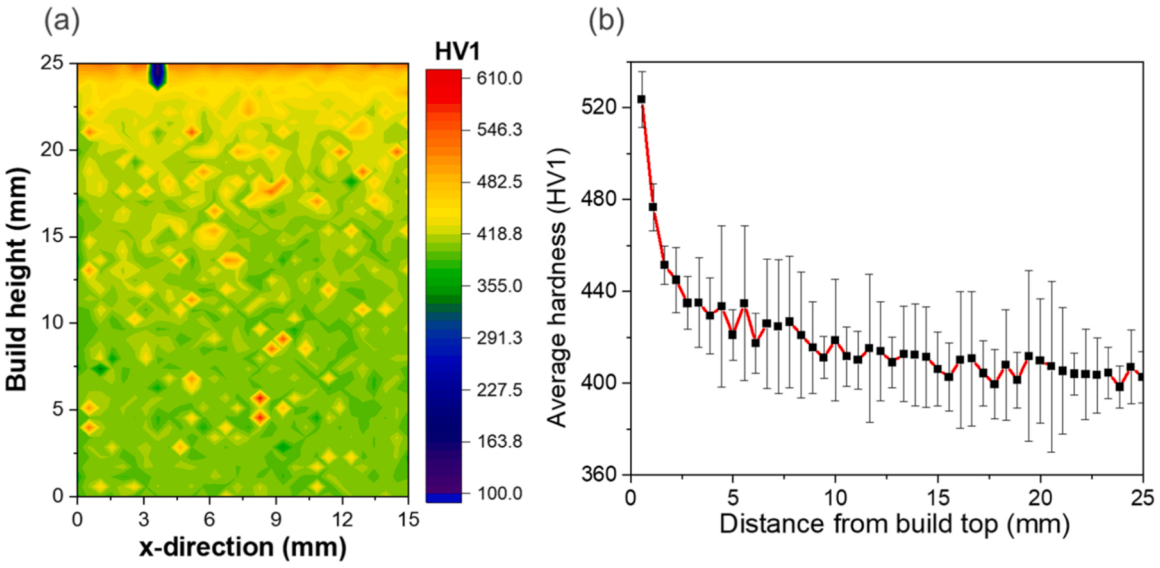

Fig. 3. (a) Hardness maps throughout an entire X-Z cross section, as measured by HV1 microhardness testing. (b) A plot of the average hardness as a function of the build height.

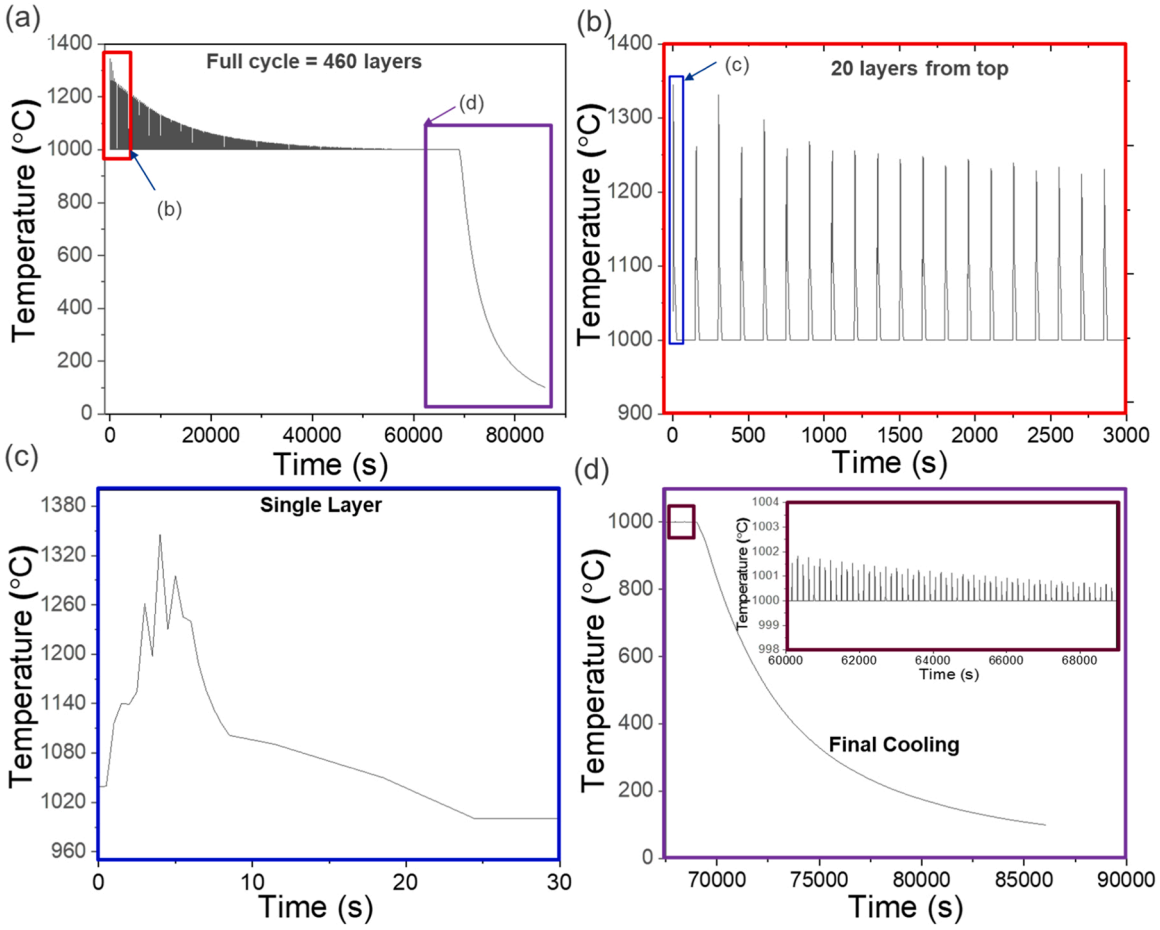

Fig. 4. Simulated thermal profile of the E-PBF build at 23 mm from the top using a semi-analytical heat conduction model. (a) Profile for 460 layers. (b) Magnified region of (a) to show the first 20 layers from the top. (c) Magnified region of (b) to show a single layer (1st layer only). (d) Time taken for the build to cool after the last layer deposition.

magnified view of 5a showing the simulated phase fraction at the center points of the top 70 layers, whereas Fig. 5c corresponds to the first two layers from the top. As mentioned earlier, the top layer (460th layer) represents the microstructure after solidification. The microstructure of the layers below is determined by the number of thermal cycles, which increases with distance to the top. For example, layers 459, 458, 457, up

Table 3
Computational parameters used in the simulation.

Precipitation domain	γ
Nucleation site γ′	Bulk (homogenous)
Nucleation site MC carbide	Bulk (Homogenous)
Precipitates class size	250
Regular solution critical temperature γ′	2500 K[64]
Calculated interfacial energy	γ′ = 0.080–0.140 J/m^2 and MC carbide = 0.410–0.430 J/m^2

to layer 1 (region of interest) experience 1, 2, 3 and 459 thermal cycles, respectively. In the top layer in Fig. 5c, the volume fraction of γ′ and carbides increases with temperature. For γ′, it decreases to zero when the temperature is above the solvus temperature after a few seconds. Carbides, however, remain constant in their volume fraction reaching equilibrium (phase fraction ~ 0.9%) in a short time. The topmost layer can be compared to the first deposit, and the peak in temperature symbolizes the stage where the electron beam heats the powder until melting. This means γ′ and carbide precipitation might have started in the powder particles during heating from the build temperature and electron beam until the onset of melting, where γ′ dissolves, but carbides remain stable [28].

During cooling after deposition, γ′ reprecipitates at a temperature of 1085 °C, which is below its solvus temperature. As cooling progresses, the phase fraction increases steadily to ~27% and remains constant at 1000 °C (elevated build temperature). The calculated equilibrium fraction of phases by MatCalc is used to show the complex precipitation characteristics in this alloy. Fig. 6 shows that MC carbides form during solidification at 1320 °C, followed by γ′, which precipitate when the solidified layer cools to 1140 °C. This indicates that all deposited layers might contain a negligible amount of these precipitates before subsequent layer deposition, while being at the 1000 °C build temperature or during cooling to RT. The phase diagram also shows that the equilibrium fraction of the γ′ increases as temperature decreases. For instance, at 1000, 900, and 800 °C, the phase fractions are ~30%, 38%, and 42%, respectively.

Deposition of subsequent layers causes previous layers to undergo phase transformations as they are exposed to several thermal cycles with different peak temperatures. In Fig. 5c, as the subsequent layer is being deposited, γ′ in the previous layer (459th layer) begins to dissolve as the temperature crosses the solvus temperature. This is witnessed by the reduction of the γ′ phase fraction. This graph also shows how this phase dissolves during heating. However, the phase fraction of MC carbide remains stable at high temperatures and no dissolution is seen during thermal cycling. Upon cooling, the γ′ that was dissolved during heating reprecipitates with a surge in the phase fraction until 1000 °C, after which it remains constant. This microstructure is similar to the solidification microstructure (layer 460), with a similar γ′ phase fraction (~27%).

The complete dissolution and reprecipitation of γ′ continue for

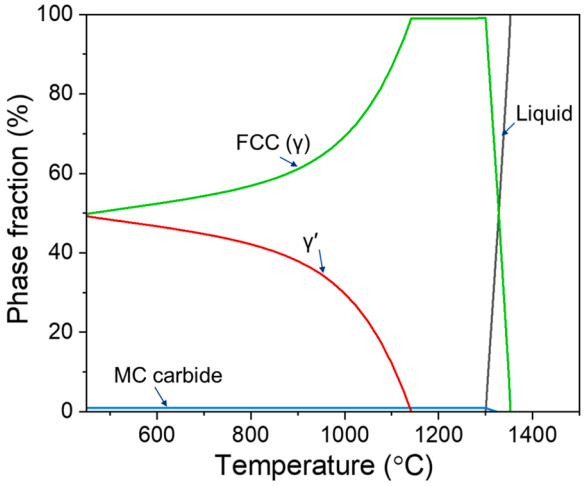

Fig. 6. Calculated equilibrium fraction of phases in IN738 using MatCalc.

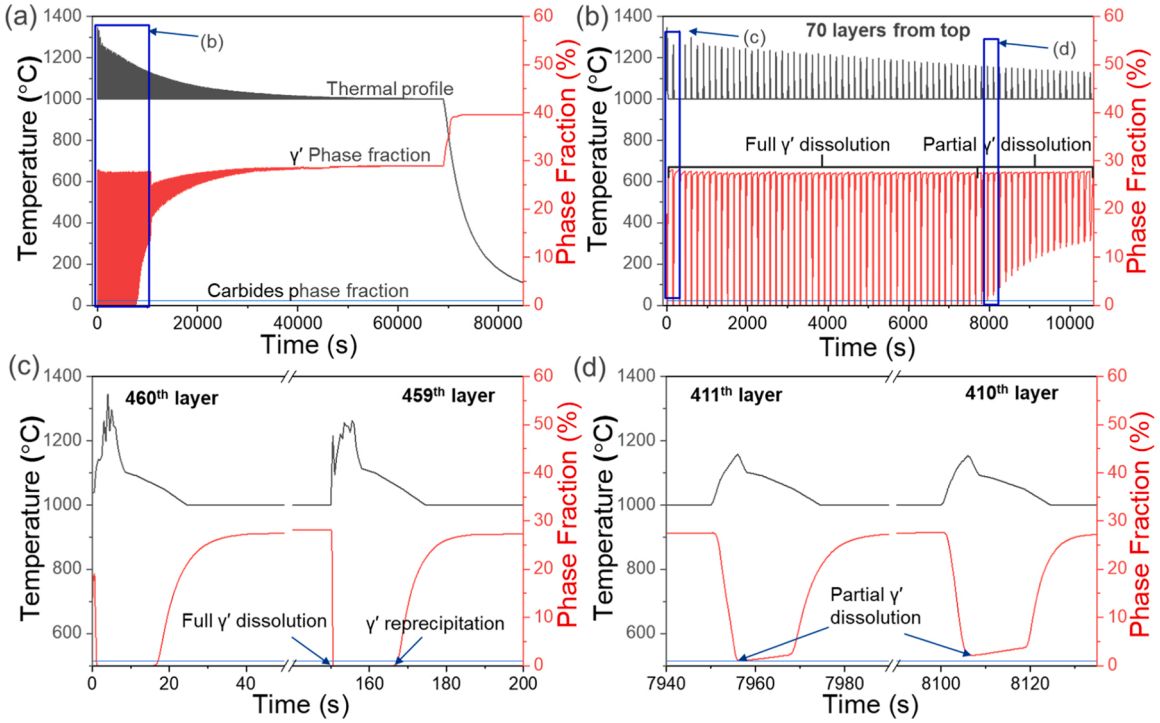

Fig. 5. Simulated phase fractions of γ′ and MC carbide during thermal cycling at 2 mm from the bottom. (a) Full cycle. (b) First 70 layers from top. (c) First 2 layers from the top (layer 460 and 459). (d) Layer 411 and 410.

several cycles until the 50th layer from the top (layer 411), where the phase fraction does not reach zero during heating to the peak temperature (see Fig. 5d). This indicates the 'partial' dissolution of γ′, which continues progressively with additional layers. It should be noted that the peak temperatures for layers that underwent complete dissolution were much higher (1170–1300 °C) than the γ′ solvus.

The dissolution and reprecipitation of γ′ during thermal cycling are further confirmed in Fig. 7, which summarizes the nucleation rate, phase fraction, and concentration of major elements that form γ′ in the matrix. Fig. 7b magnifies a single layer (3rd layer from top) within the full dissolution region in Fig. 7a to help identify the nucleation and growth mechanisms. From Fig. 7b, γ′ nucleation begins during cooling whereby the nucleation rate increases to reach a maximum value of approximately 1×10^{20} $m^{-3}s^{-1}$. This fast kinetics implies that some rearrangement of atoms is required for γ′ precipitates to form in the matrix [65,66]. The matrix at this stage is in a non-equilibrium condition. Its composition is similar to the nominal composition and remains unchanged. The phase fraction remains insignificant at this stage although nucleation has started. The nucleation rate starts declining upon reaching the peak value. Simultaneously, diffusion-controlled growth of existing nuclei occurs, depleting the matrix of γ′ forming elements (Al and Ti). Thus, from Eqs. (7) and (11), ΔG_{vol} continuously decreases until nucleation ceases. The growth of nuclei is witnessed by the increase in phase fraction until a constant level is reached at 27% upon cooling to and holding at build temperature. This nucleation event is repeated several times.

At the onset of partial dissolution, the nucleation rate jumps to 1×10^{21} $m^{-3}s^{-1}$, and then reduces sharply at the middle stage of partial dissolution. The nucleation rate reaches 0 at a later stage. Supplementary Fig. S1 shows a magnified view of the nucleation rate, phase fraction, and thermal profile, underpinning this trend. The jump in nucleation rate at the onset is followed by a progressive reduction in the solute content of the matrix. The peak temperatures (~1130–1160 °C) are lower than those in complete dissolution regions but still above or close to the γ′ solvus. The maximum phase fraction (~27%) is similar to that of the complete dissolution regions. At the middle stage, the reduction in nucleation rate is accompanied by a sharp drop in the matrix composition. The γ′ fraction drops to ~24%, where the peak temperatures of the layers are just below or at γ′ solvus. The phase fraction then increases progressively through the later stage of partial dissolution to ~30% towards the end of thermal cycling. The matrix solute content continues to drop although no nucleation event is seen. The peak temperatures are then far below the γ′ solvus. It should be noted that the matrix concentration after complete dissolution remains constant. Upon cooling to RT after final layer deposition, the nucleation rate increases again, indicating new nucleation events. The phase fraction reaches ~40%, with a further depletion of the matrix in major γ′ forming elements.

3.3.2.2. γ′ size distribution. Fig. 8 shows histograms of the γ′ precipitate size distributions (PSD) along the build height during deposition. These PSDs are predicted at the end of each layer of interest just before final cooling to room temperature, to separate the role of thermal cycles from final cooling on the evolution of γ′. The PSD for the top layer (layer 460) is shown in Fig. 8a (last solidified region with solidification microstructure). The γ′ size ranges from 120 to 230 nm and is similar to the 44 layers below (2.2 mm from the top).

Further down the build, γ′ begins to coarsen after layer 417 (44th layer from top). Fig. 8c shows the PSD after the 44th layer, where the γ′ size exhibits two peaks at ~120–230 and ~300 nm, with most of the population being in the former range. This is the onset of partial dissolution where simultaneously with the reprecipitation and growth of fresh γ′, the undissolved γ′ grows rapidly through diffusive transport of atoms to the precipitates. This is shown in Fig. 8c, where the precipitate class sizes between 250 and 350 represent the growth of undissolved γ′. Although this continues in the 416th layer, the phase fractions plot indicates that the onset of partial dissolution begins after the 411th layer. This implies that partial dissolution started early, but the fraction of undissolved γ′ was too low to impact the phase fraction. The reprecipitated γ′ are mostly in the 100–220 nm class range and similar to those

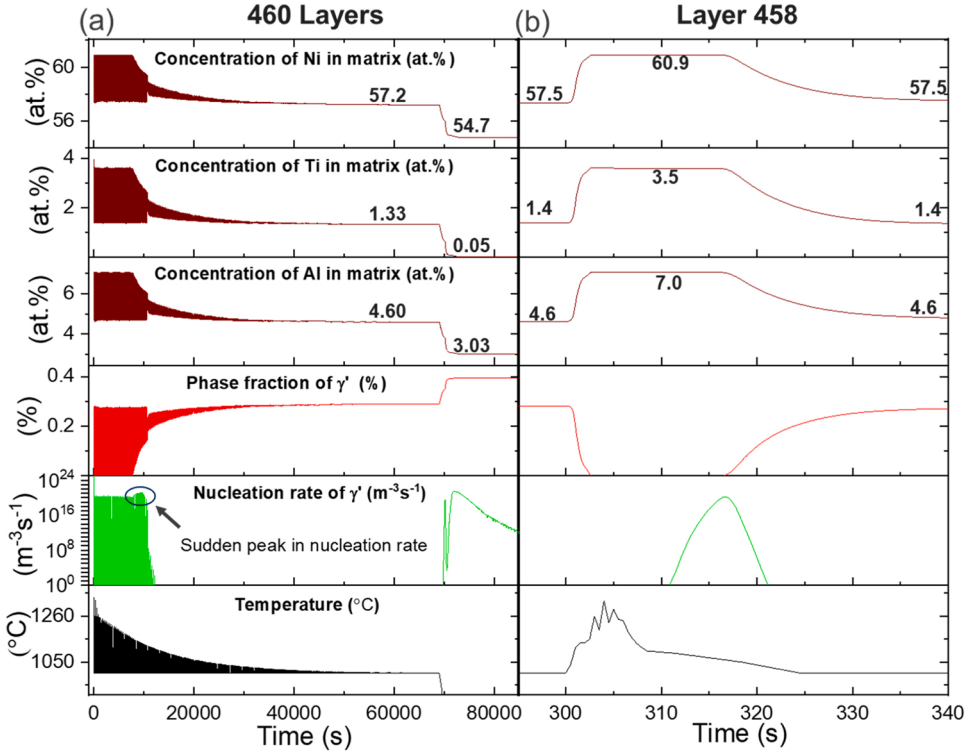

Fig. 7. Correlation of concentration of major γ′ forming elements in the matrix, phase fraction, γ′ nucleation rate, and temperature during thermal cycling. (a) Thermal profile for 460 layers. (b) Magnified region of (a) to show a single layer (3rd layer from top, equivalent to layer 458).

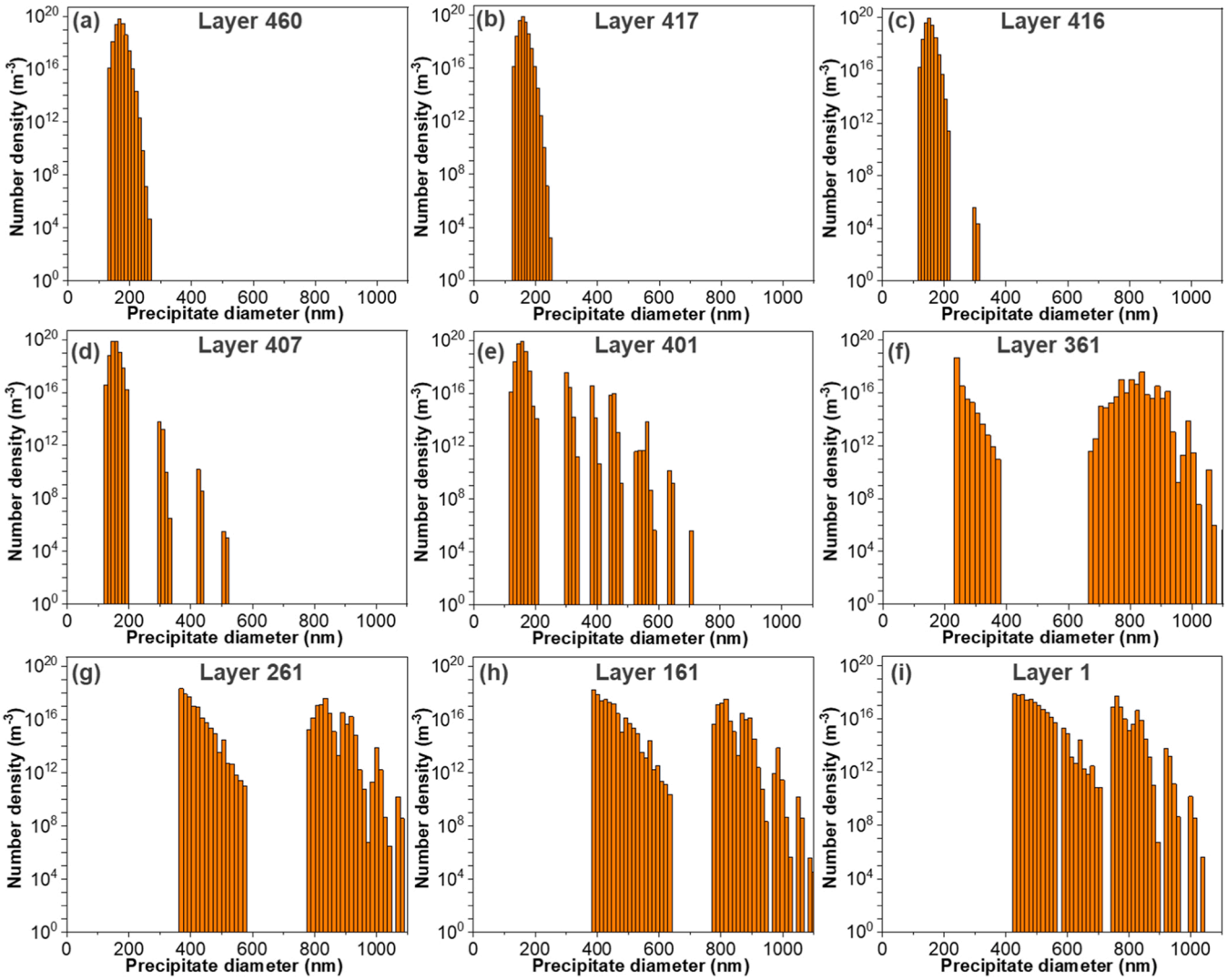

Fig. 8. Histograms of γ′ size distributions at different positions along the build height during deposition just before cooling to room temperature begins.

observed during full dissolution.

As the number of layers increases, coarsening intensifies with continued growth of more undissolved γ′, and reprecipitation and growth of partially dissolved ones. Fig. 8d, e, and f show this sequence. Further down the build, coarsening progresses rapidly, as shown in Figs. 8d, 8e, and 8f. The γ′ size ranges from 120 to 1100 nm, with the peaks at 160, 180, and 220 nm in Figs. 8d, 8e, and 8f, respectively. Coarsening continues until nucleation ends during dissolution, where only the already formed γ′ precipitates continue to grow during further thermal cycling. The γ′ size at this point is much larger, as observed in layers 361 and 261, and continues to increase steadily towards the bottom (layer 1). Two populations in the ranges of ~380–700 and ~750–1100 nm, respectively, can be seen. The steady growth of γ′ towards the bottom is confirmed by the gradual decrease in the concentration of solute elements in the matrix (Fig. 7a). It should be noted that for each layer, the γ′ class with the largest size originates from continuous growth of the earliest set of the undissolved precipitates.

Figs. 9, 10 and supplementary Figs. S2 and S3 show the γ′ size evolution during heating and cooling of a single layer in the full dissolution region, and early, middle stages, and later stages of partial dissolution, respectively. In all, the size of γ′ reduces during layer heating. Depending on the peak temperature of the layer which varies with build height, γ′ are either fully or partially dissolved as mentioned earlier. Upon cooling, the dissolved γ′ reprecipitate.

In Fig. 9, those layers that underwent complete dissolution (top layers) were held above γ′ solvus temperature for longer. In Fig. 10, layers at the early stage of partial dissolution spend less time in the γ′ solvus temperature region during heating, leading to incomplete dissolution. In such conditions, smaller precipitates are fully dissolved while larger ones shrink [67]. Layers in the middle stages of partial dissolution have peak temperatures just below or at γ′ solvus, not sufficient to achieve significant γ′ dissolution. As seen in supplementary Fig. S2, only a few smaller γ′ are dissolved back into the matrix during heating, i.e., growth of precipitates is more significant than dissolution. This explains the sharp decrease in concentration of Al and Ti in the matrix in this layer.

The previous sections indicate various phenomena such as an increase in phase fraction, further depletion of matrix composition, and new nucleation bursts during cooling. Analysis of the PSD after the final cooling of the build to room temperature allows a direct comparison to post-printing microstructural characterization. Fig. 11 shows the γ′ size distribution of layer 1 (460th layer from the top) after final cooling to room temperature. Precipitation of secondary γ′ is observed, leading to the multimodal size distribution of secondary and primary γ′. The secondary γ′ size falls within the 10–80 nm range. As expected, a further growth of the existing primary γ′ is also observed during cooling.

3.3.2.3. γ′ chemistry after deposition. Fig. 12 shows the concentration of

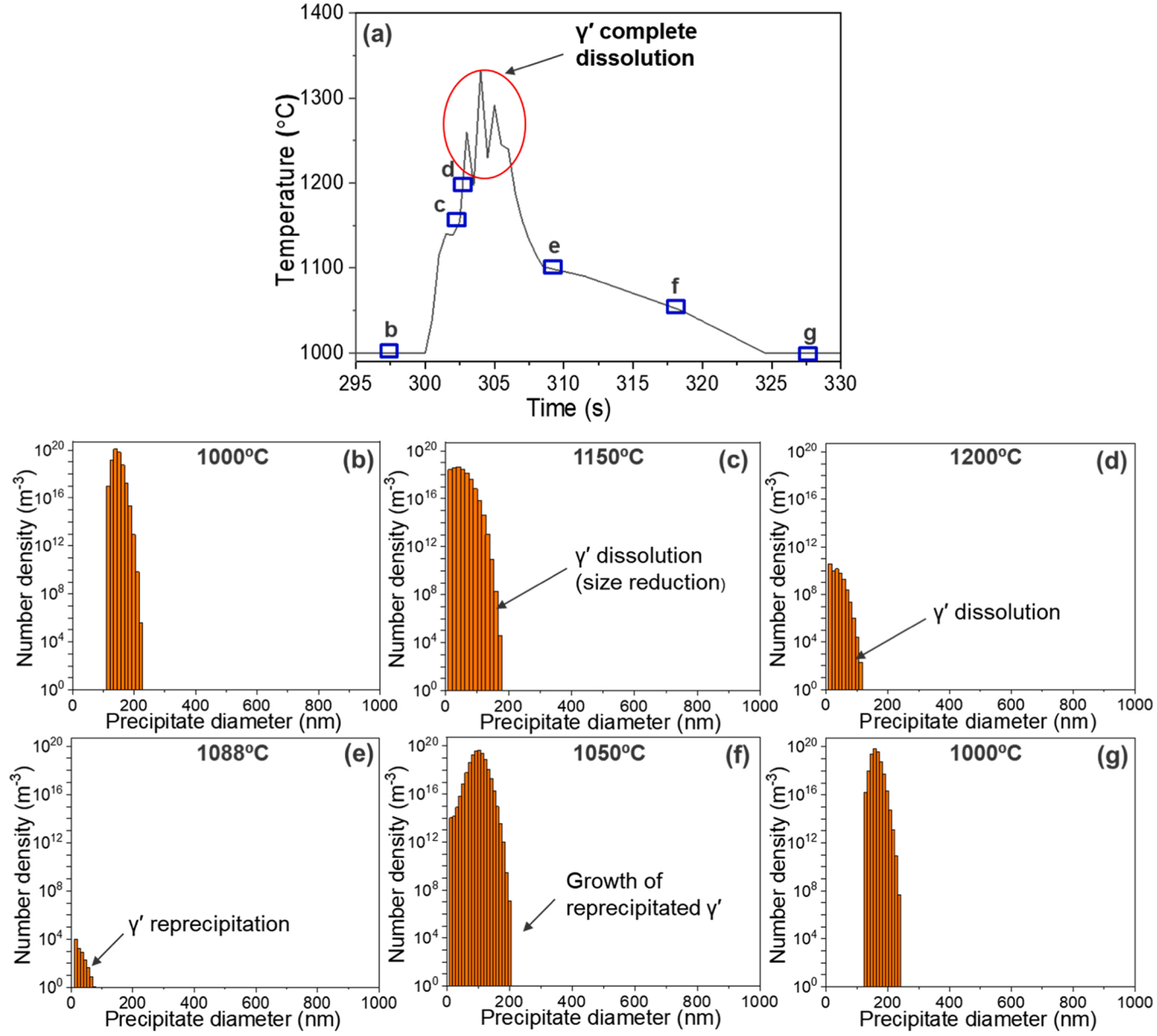

Fig. 9. γ′ size evolution during heating and cooling of a single layer in the full dissolution region. (a) Thermal profile of a single layer. γ′ size distribution: (b) upon holding at the elevated build temperature before subsequent layer deposition, (c, d) Upon dissolution of γ′ indicated by size reduction during deposition of further layers. Full dissolution occurs after 1200°C. (e) Upon re-precipitation of dissolved γ′ and (f, g) upon growth of re-precipitated γ′.

the major elements that form γ′ (Al, Ti, and Ni) in the primary and secondary γ′ at the bottom of the build, as calculated by MatCalc. The secondary γ′ has a higher Al content (13.5–14.5 at% Al), compared to 13 at% Al in the primary γ′. Additionally, within the secondary γ′, the smallest particles (~10 nm) have higher Al contents than larger ones (~70 nm). In contrast, for the primary γ′, there is no significant variation in the Al content as a function of their size. The Ni concentration in secondary γ′ (71.1–72 at%) is also higher in comparison to the primary γ′ (70 at%). The smallest secondary γ′ (~10 nm) have higher Ni contents than larger ones (~70 nm), whereas there is no substantial change in the Ni content of primary γ′, based on their size. As expected, Ti shows an opposite size-dependent variation. It ranges from ~ 7.7–8.7 at% Ti in secondary γ′ to ~9.2 at% in primary γ′. Similarly, within the secondary γ′, the smallest (~10 nm) have lower Al contents than the larger ones (~70 nm). No significant variation is observed for Ti content in primary γ′.

4. Discussion

A combined modelling method is utilized to study the microstructural evolution during E-PBF of IN738. The presented results are discussed by examining the precipitation and dissolution mechanism of γ′ during thermal cycling. This is followed by a discussion on the phase fraction and size evolution of γ′ during thermal cycling and after final cooling. A brief discussion on carbide morphology is also made. Finally, a comparison is made between the simulation and experimental results to assess their agreement.

4.1. γ′ morphology as a function of build height

4.1.1. Nucleation of γ′

The fast precipitation kinetics of the γ′ phase enables formation of γ′ upon quenching from higher temperatures (above solvus) during thermal cycling [66]. In Fig. 7b, for a single layer in the full dissolution

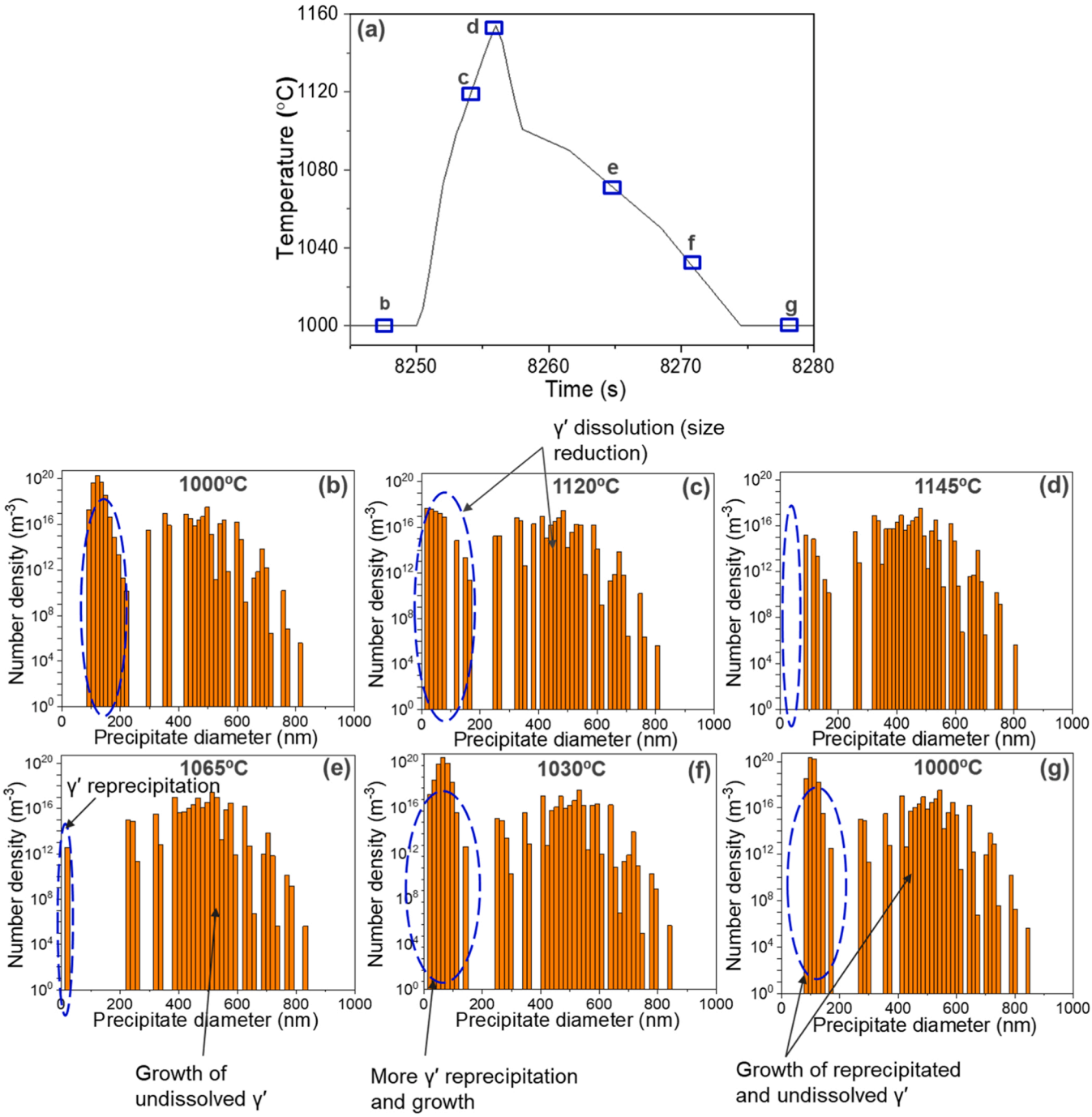

Fig. 10. γ′ size evolution during heating and cooling of a single layer in the early stages of the partial dissolution region. (a) Thermal profile of a single layer. γ′ size distribution: (b) upon holding at the elevated build temperature before subsequent layer deposition. Two different precipitate classes are seen. (c) Upon dissolution of γ′ indicated by size reduction. Smaller γ′ dissolve more rapidly than larger ones. (d) Upon complete dissolution of the smaller γ′ precipitate class, (e) upon re-precipitation of dissolved γ′ and growth of undissolved ones, (f) upon further γ′ re-precipitation, growth of precipitated γ′ and undissolved ones, and (g) upon further growth of re-precipitated γ′ and undissolved ones.

region, during cooling, the initial increase in nucleation rate signifies the first formation of nuclei. The slight increase in nucleation rate during partial dissolution, despite a decrease in the concentration of γ′ forming elements, may be explained by the nucleation kinetics. During partial dissolution and as the precipitates shrink, it is assumed that the regions at the vicinity of partially dissolved precipitates are enriched in γ′ forming elements [68,69]. This differs from the full dissolution region, in which case the chemical composition is evenly distributed in the matrix. Several authors have attributed the solute supersaturation of the matrix around primary γ′ to partial dissolution during isothermal ageing [69–72]. The enhanced supersaturation in the regions close to the precipitates results in a much higher driving force for nucleation, leading to a higher nucleation rate upon cooling. This phenomenon can be closely related to the several nucleation bursts upon continuous cooling of Ni-based superalloys, where second nucleation bursts exhibit higher nucleation rates [38,68,73,74].

At middle stages of partial dissolution, the reduction in the nucleation rate indicates that the existing composition and low supersaturation did not trigger nucleation as the matrix was closer to the equilibrium state. The end of a nucleation burst means that the

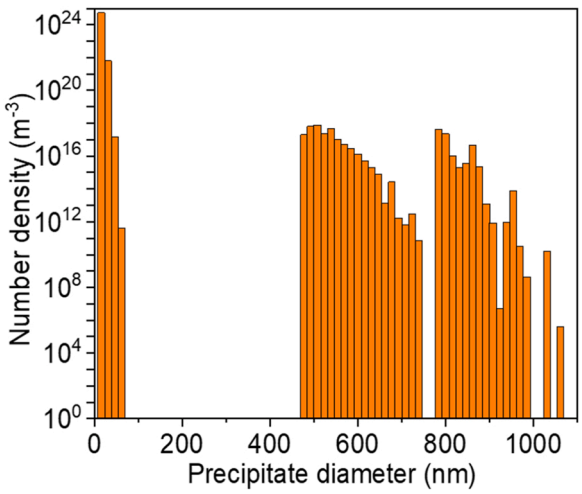

Fig. 11. Histogram of γ′ size distribution of layer 1 after final cooling to RT.

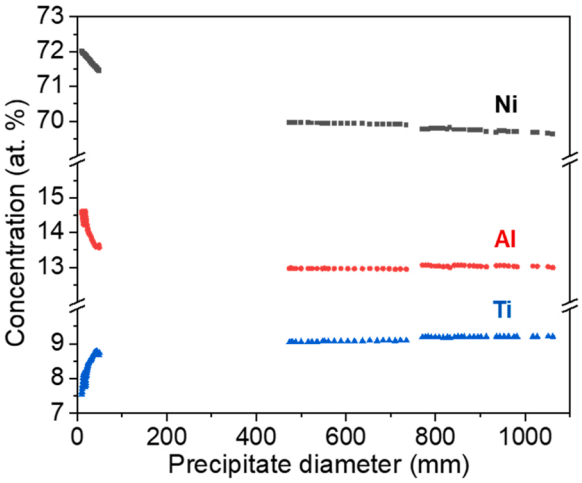

Fig. 12. Al, Ti, and Ni content variations as a function of precipitate diameter after final cooling to RT predicted by MatCalc.

supersaturation of Al and Ti has reached a low level, incapable of providing sufficient driving force during cooling to or holding at 1000 °C for further nucleation [73]. Earlier studies on Ni-based superalloys have reported the same phenomenon during ageing or continuous cooling from the solvus temperature to RT [38,73,74].

4.1.2. Dissolution of γ′ during thermal cycling

γ′ dissolution kinetics during heating are fast when compared to nucleation due to exponential increase in phase transformation and diffusion activities with temperature [65]. As shown in Figs. 9, 10, and supplementary Figs. S2 and S3, the reduction in γ′ phase fraction and size during heating indicates γ′ dissolution. This is also revealed in Fig. 5 where phase fraction decreases upon heating. The extent of γ′ dissolution mostly depends on the temperature, time spent above γ′ solvus, and precipitate size [75–77]. Smaller γ′ precipitates are first to be dissolved [67,77,78]. This is mainly because more solute elements need to be transported away from large γ′ precipitates than from smaller ones [79]. Also, a high temperature above γ′ solvus temperature leads to a faster dissolution rate [80]. The equilibrium solvus temperature of γ′ in IN738 in our MatCalc simulation (Fig. 6) and as reported by Ojo et al. [47] is 1140 °C and 1130–1180 °C, respectively. This means the peak temperature experienced by previous layers decreases progressively from γ′ supersolvus to subsolvus, near-solvus, and far from solvus as the number of subsequent layers increases. Based on the above, it can be inferred that the degree of dissolution of γ′ contributes to the gradient in precipitate distribution.

Although the peak temperatures during later stages of partial dissolution are much lower than the equilibrium γ′ solvus, γ′ dissolution still occurs but at a significantly lower rate (supplementary Fig. S3). Wahlmann et al. [28] also reported a similar case where they observed the rapid dissolution of γ′ in CMSX-4 during fast heating and cooling cycles at temperatures below the γ′ solvus. They attributed this to the γ′ phase transformation process taking place in conditions far from the equilibrium. While the same reasoning may be valid for our study, we further believe that the greater surface area to volume ratio of the small γ′ precipitates contributed to this. This ratio means a larger area is available for solute atoms to diffuse into the matrix even at temperatures much below the solvus [81].

4.2. γ′ phase fraction and size evolution

4.2.1. During thermal cycling

In the first layer, the steep increase in γ′ phase fraction during heating (Fig. 5), which also represents γ′ precipitation in the powder before melting, has qualitatively been validated in [28]. The maximum phase fraction of 27% during the first few layers of thermal cycling indicates that IN738 theoretically could reach the equilibrium state (~30%), but the short interlayer time at the build temperature counteracts this. The drop in phase fraction at middle stages of partial dissolution is due to the low number of γ′ nucleation sites [73]. It has been reported that a reduction of γ′ nucleation sites leads to a delay in obtaining the final volume fraction as more time is required for γ′ precipitates to grow and reach equilibrium [82]. This explains why even upon holding for 150 s before subsequent layer deposition, the phase fraction does not increase to those values that were observed in the previous full γ′ dissolution regions. Towards the end of deposition, the increase in phase fraction to the equilibrium value of 30% is as a result of the longer holding at build temperature or close to it [83].

During thermal cycling, γ′ particles begin to grow immediately after they first precipitate upon cooling. This is reflected in the rapid increase in phase fraction and size during cooling in Fig. 5 and supplementary Fig. S2, respectively. The rapid growth is due to the fast diffusion of solute elements at high temperatures [84]. The similar size of γ′ for the first 44 layers from the top can be attributed to the fact that all layers underwent complete dissolution and hence, experienced the same nucleation event and growth during deposition. This corresponds with the findings by Balikci et al. [85], who reported that the degree of γ′ precipitation in IN738LC does not change when a solution heat treatment is conducted above a certain critical temperature.

The increase in coarsening rate (Fig. 8) during thermal cycling can first be ascribed to the high peak temperature of the layers [86]. The coarsening rate of γ′ is known to increase rapidly with temperature due to the exponential growth of diffusion activity. Also, the simultaneous dissolution with coarsening could be another reason for the high coarsening rate, as γ′ coarsening is a diffusion-driven process where large particles grow by consuming smaller ones [78,84,86,87]. The steady growth of γ′ towards the bottom of the build is due to the much lower layer peak temperature, which is almost close to the build temperature, and reduced dissolution activity, as is seen in the much lower solute concentration in γ′ compared to those in the full and partial dissolution regions.

4.2.2. During cooling

The much higher phase fraction of ~40% upon cooling signifies the tendency of γ′ to reach equilibrium at lower temperatures (Fig. 4). This is due to the precipitation of secondary γ′ and a further increase in the size of existing primary γ′, which leads to a multimodal size distribution of γ′ after cooling [38,73,88–90]. The reason for secondary γ′ formation during cooling is as follows: As cooling progresses, it becomes increasingly challenging to redistribute solute elements in the matrix owing to

their lower mobility [38,73]. A higher supersaturation level in regions away from or free of the existing γ′ precipitates is achieved, making them suitable sites for additional nucleation bursts. More cooling leads to the growth of these secondary γ′ precipitates, but as the temperature and in turn, the solute diffusivity is low, growth remains slow.

4.3. Carbides

MC carbides in IN738 are known to have a significant impact on the high-temperature strength. They can also act as effective hardening particles and improve the creep resistance [91]. Precipitation of MC carbides in IN738 and several other superalloys is known to occur during solidification or thermal treatments (e.g., hot isostatic pressing) [92]. In our case, this means that the MC carbides within the E-PBF build formed because of the thermal exposure from the E-PBF thermal cycle in addition to initial solidification. Our simulation confirms this as MC carbides appear during layer heating (Fig. 5). The constant and stable phase fraction of MC carbides during thermal cycling can be attributed to their high melting point (~1360 °C) and the short holding time at peak temperatures [75,93,94]. The solvus temperature for most MC carbides exceeds most of the peak temperatures observed in our simulation, and carbide dissolution kinetics at temperatures above the solvus are known to be comparably slow [95]. The stable phase fraction and random distribution of MC carbides signifies the slight influence on the gradient in hardness.

4.4. Comparison of simulations and experiments

4.4.1. Precipitate phase fraction and morphology as a function of build height

A qualitative agreement is observed for the phase fraction of carbides, i.e. ~0.8% in the experiment and ~0.9% in the simulation. The phase fraction of γ′ differs, with the experiment reporting a value of ~51% and the simulation, 40%. Despite this, the size distribution of primary γ′ along the build shows remarkable consistency between experimental and computational analyses. It is worth noting that the primary γ′ morphology in the experimental analysis is observed in the as-fabricated state, whereas the simulation (Fig. 8) captures it during deposition process. The primary γ′ size in the experiment is expected to experience additional growth during the cooling phase. Regardless, both show similar trends in primary γ′ size increments from the top to the bottom of the build. The larger primary γ' size in the simulation versus the experiment can be attributed to the fact that experimental and simulation results are based on 2D and 3D data, respectively. The absence of stereological considerations [96] in our analysis could have led to an underestimation of the precipitate sizes from SEM measurements. The early starts of coarsening (8th layer) in the experiment compared to the simulation (45th layer) can be attributed to a higher actual γ′ solvus temperature than considered in our simulation [47]. The solvus temperature of γ′ in a Ni-based superalloy is mainly determined by the detailed composition. A high amount of Cr and Co are known to reduce the solvus temperature, whereas Ta and Mo will increase it [97–99]. The elemental composition from our experimental work was used for the simulation except for Ta. It should be noted that Ta is not included in the thermodynamic database in MatCalc used, and this may have reduced the solvus temperature. This could also explain the relatively higher γ′ phase fraction in the experiment than in simulation, as a higher γ′ solvus temperature will cause more γ′ to precipitate and grow early during cooling [99,100].

Another possible cause of this deviation can be attributed to the extent of γ′ dissolution, which is mainly determined by the peak temperature. It can be speculated that individual peak temperatures at different layers in the simulation may have been over-predicted. However, one needs to consider that the true thermal profile is likely more complicated in the actual E-PBF process [101]. For example, the current model assumes that the thermophysical properties of the material are temperature-independent, which is not realistic. Many materials, including IN738, exhibit temperature-dependent properties such as thermal conductivity, specific heat capacity, and density [102]. This means that heat transfer simulations may underestimate or overestimate the temperature gradients and cooling rates within the powder bed and the solidified part. Additionally, the model does not account for the reduced thermal diffusivity through unmelted powder, where gas separating the powder acts as insulation, impeding the heat flow [1]. In E-PBF, the unmelted powder regions with trapped gas have lower thermal diffusivity compared to the fully melted regions, leading to localized temperature variations, and altered solidification behavior. These limitations can impact the predictions, particularly in relation to the carbide dissolution, as the peak temperatures may be underestimated.

While acknowledging these limitations, it is worth emphasizing that achieving a detailed and accurate representation of each layer's heat source would impose tough computational challenges. Given the substantial layer count in E-PBF, our decision to employ a semi-analytical approximation strikes a balance between computational feasibility and the capture of essential trends in thermal profiles across diverse build layers. In future work, a dual-calibration strategy is proposed to further reduce simulation-experiment disparities. By refining temperature-independent thermophysical property approximations and absorptivity in the heat source model, and by optimizing interfacial energy descriptions in the kinetic model, the predictive precision could be enhanced. Further refining the simulation controls, such as adjusting the precipitate class size may enhance quantitative comparisons between modeling outcomes and experimental data in future work.

4.4.2. Multimodal size distribution of γ′ and concentration

Another interesting feature that sees qualitative agreement between the simulation and the experiment is the multimodal size distribution of γ′. The formation of secondary γ′ particles in the experiment and most E-PBF Ni-based superalloys is suggested to occur at low temperatures, during final cooling to RT [16,73,90]. However, so far, this conclusion has been based on findings from various continuous cooling experiments, as the study of the evolution during AM would require an in-situ approach. Our simulation unambiguously confirms this in an AM context by providing evidence for secondary γ′ precipitation during slow cooling to RT. Additionally, it is possible to speculate that the chemical segregation occurring during solidification, due to the preferential partitioning of certain elements between the solid and liquid phases, can contribute to the multimodal size distribution during deposition [51]. This is because chemical segregation can result in variations in the local composition of superalloys, which subsequently affects the nucleation and growth of γ′. Regions with higher concentrations of alloying elements will encourage the formation of larger γ′ particles, while regions with lower concentrations may favor the nucleation of smaller precipitates. However, it is important to acknowledge that the elevated temperature during the E-PBF process will largely homogenize these compositional differences [103,104].

A good correlation is also shown in the composition of major γ′ forming elements (Al and Ti) in primary and secondary γ′. Both experiment and simulation show an increasing trend for Al content and a decreasing trend for Ti content from primary to secondary γ′. The slight composition differences between primary and secondary γ′ particles are due to the different diffusivity of γ′ stabilizers at different thermal conditions [105,106]. As the formation of multimodal γ′ particles with different sizes occurs over a broad temperature range, the phase chemistry of γ′ will be highly size dependent. The changes in the chemistry of various γ′ (primary, secondary, and tertiary) have received significant attention since they have a direct influence on the performance [68,105,107–109]. Chen et al. [108,109], reported a high Al content in the smallest γ′ precipitates compared to the largest, while Ti showed an opposite trend during continuous cooling in a RR1000 Ni-based superalloy. This was attributed to the temperature and cooling

rate at which the γ′ precipitates were formed. The smallest precipitates formed last, at the lowest temperature and cooling rate. A comparable observation is evident in the present investigation, where the secondary γ′ forms at a low temperature and cooling rate in comparison to the primary. The temperature dependence of γ′ chemical composition is further evidenced in supplementary Fig. S4, which shows the equilibrium chemical composition of γ′ as a function of temperature.

5. Conclusions

A correlative modelling approach capable of predicting solid-state phase transformations kinetics in metal AM was developed. This approach involves computational simulations with a semi-analytical heat transfer model and the MatCalc thermo-kinetic software. The method was used to predict the phase transformation kinetics and detailed morphology and chemistry of γ′ and MC during E-PBF of IN738 Ni-based superalloy. The main conclusions are:

1. The computational simulations are in qualitative agreement with the experimental observations. This is particularly true for the γ′ size distribution along the build height, the multimodal size distribution of particles, and the phase fraction of MC carbides.
2. The deviations between simulation and experiment in terms of γ′ phase fraction and location in the build are most likely attributed to a higher γ′ solvus temperature during the experiment than in the simulation, which is argued to be related to the absence of Ta in the MatCalc database.
3. The dissolution and precipitation of γ′ occur fast and under non-equilibrium conditions. The level of γ′ dissolution determines the gradient in γ′ size distribution along the build. After thermal cycling, the final cooling to room temperature has further significant impacts on the final γ′ size, morphology, and distribution.
4. A negligible amount of γ′ forms in the first deposited layer before subsequent layer deposition, and a small amount of γ′ may also form in the powder induced by the 1000 °C elevated build temperature before melting.

Our findings confirm the suitability of MatCalc to predict the microstructural evolution at various positions throughout a build in a Ni-based superalloy during E-PBF. It also showcases the suitability of a tool which was originally developed for traditional thermo-mechanical processing of alloys to the new additive manufacturing context. Our simulation capabilities are likely extendable to other alloy systems that undergo solid-state phase transformations implemented in MatCalc (various steels, Ni-based superalloys, and Al-alloys amongst others) as well as other AM processes such as L-DED and L-PBF which have different thermal cycle characteristics. New tools to predict the microstructural evolution and properties during metal AM are important as they provide new insights into the complexities of AM. This will enable control and design of AM microstructures towards advanced materials properties and performances.

CRediT authorship contribution statement

Primig Sophie: Writing – review & editing, Supervision, Resources, Project administration, Funding acquisition, Conceptualization. **Adomako Nana Kwabena:** Writing – original draft, Writing – review & editing, Visualization, Software, Investigation, Formal analysis, Conceptualization. **Haghdadi Nima:** Writing – review & editing, Supervision, Project administration, Methodology, Conceptualization. **Dingle James F.L.:** Methodology, Conceptualization, Software, Writing – review & editing, Visualization. **Kozeschnik Ernst:** Writing – review & editing, Software, Methodology. **Liao Xiaozhou:** Writing – review & editing, Project administration, Funding acquisition. **Ringer Simon P:** Writing – review & editing, Project administration, Funding acquisition.

Declaration of Competing Interest

The authors declare that they have no known competing financial interests or personal relationships that could have appeared to influence the work reported in this paper.

Data Availability

Data will be made available on request.

Acknowledgements

This research was sponsored by the Department of Industry, Innovation, and Science under the auspices of the AUSMURI program – which is a part of the Commonwealth's Next Generation Technologies Fund. The authors acknowledge the facilities and the scientific and technical assistance at the Electron Microscope Unit (EMU) within the Mark Wainwright Analytical Centre (MWAC) at UNSW Sydney and Microscopy Australia. Nana Adomako is supported by a UNSW Scientia PhD scholarship. Michael Haines' (UNSW Sydney) contribution to the revised version of the original manuscript is thankfully acknowledged.

Appendix A. Supporting information

Supplementary data associated with this article can be found in the online version at doi:10.1016/j.addma.2023.103771.

References

[1] T. Debroy, H.L. Wei, J.S. Zuback, T. Mukherjee, J.W. Elmer, J.O. Milewski, A. M. Beese, A. Wilson-heid, A. De, W. Zhang, Additive manufacturing of metallic components – process, structure and properties, Prog. Mater. Sci. 92 (2018) 112–224, https://doi.org/10.1016/j.pmatsci.2017.10.001.

[2] S. Li, Q. Wei, Y. Shi, C.K. Chua, Z. Zhu, D. Zhang, Microstructure characteristics of Inconel 625 superalloy manufactured by selective laser melting, J. Mater. Sci. Technol. 31 (2015) 946–952, https://doi.org/10.1016/j.jmst.2014.09.020.

[3] M. Gäumann, C. Bezençon, P. Canalis, W. Kurz, Single-crystal laser deposition of superalloys: processing-microstructure maps, Acta Mater. 49 (2001) 1051–1062, https://doi.org/10.1016/S1359-6454(00)00367-0.

[4] N.K. Adomako, J.J. Lewandowski, B.M. Arkhurst, H. Choi, H.J. Chang, J.H. Kim, Microstructures and mechanical properties of multi-layered materials composed of Ti-6Al-4V, vanadium, and 17–4PH stainless steel produced by directed energy deposition, Addit. Manuf. 59 (2022), 103174, https://doi.org/10.1016/j.addma.2022.103174.

[5] H. Wang, Z.G. Zhu, H. Chen, A.G. Wang, J.Q. Liu, H.W. Liu, R.K. Zheng, S.M. L. Nai, S. Primig, S.S. Babu, S.P. Ringer, X.Z. Liao, Effect of cyclic rapid thermal loadings on the microstructural evolution of a CrMnFeCoNi high-entropy alloy manufactured by selective laser melting, Acta Mater. 196 (2020) 609–625, https://doi.org/10.1016/J.ACTAMAT.2020.07.006.

[6] N. Kwabena Adomako, N. Haghdadi, S. Primig, Electron and laser-based additive manufacturing of Ni-based superalloys: a review of heterogeneities in microstructure and mechanical properties, Mater. Des. 223 (2022), 111245, https://doi.org/10.1016/J.MATDES.2022.111245.

[7] S.H. Sun, Y. Koizumi, S. Kurosu, Y.P. Li, H. Matsumoto, A. Chiba, Build direction dependence of microstructure and high-temperature tensile property of Co-Cr-Mo alloy fabricated by electron beam melting, Acta Mater. 64 (2014) 154–168, https://doi.org/10.1016/j.actamat.2013.10.017.

[8] S.H. Sun, Y. Koizumi, S. Kurosu, Y.P. Li, A. Chiba, Phase and grain size inhomogeneity and their influences on creep behavior of Co-Cr-Mo alloy additive manufactured by electron beam melting, Acta Mater. 86 (2015) 305–318, https://doi.org/10.1016/j.actamat.2014.11.012.

[9] W. Xu, M. Brandt, S. Sun, J. Elambasseril, Q. Liu, K. Latham, K. Xia, M. Qian, Additive manufacturing of strong and ductile Ti-6Al-4V by selective laser melting via in situ martensite decomposition, Acta Mater. 85 (2015) 74–84, https://doi.org/10.1016/j.actamat.2014.11.028.

[10] S.S. Al-Bermani, M.L. Blackmore, W. Zhang, I. Todd, The origin of microstructural diversity, texture, and mechanical properties in electron beam melted Ti-6Al-4V, Metall. Mater. Trans. A Phys. Metall. Mater. Sci. 41 (2010) 3422–3434, https://doi.org/10.1007/s11661-010-0397-x.

[11] P.L. Stephenson, N. Haghdadi, R. DeMott, X.Z. Liao, S.P. Ringer, S. Primig, Effect of scanning strategy on variant selection in additively manufactured Ti-6Al-4V, Addit. Manuf. 36 (2020), 101581, https://doi.org/10.1016/j.addma.2020.101581.

[12] Y.K. Kim, K.A. Lee, Direct energy deposition of high strength austenitic stainless steel matrix nanocomposite with superior ductility: microstructure, tensile properties, and deformation behavior, Mater. Charact. 179 (2021), 111358, https://doi.org/10.1016/j.matchar.2021.111358.

[13] H. Helmer, A. Bauereiß, R.F. Singer, C. Körner, Erratum to: 'Grain structure evolution in Inconel 718 during selective electron beam melting' (Materials Science & Engineering A (2016) 668 (180–187 (S0921509316305536) (10.1016/j.msea.2016.05.046)), Mater. Sci. Eng. A. 676 (2016) 546, https://doi.org/10.1016/j.msea.2016.09.016.

[14] X. Wang, T. Keya, K. Chou, Build height effect on the Inconel 718 parts fabricated by selective laser melting, Procedia Manuf. 5 (2016) 1006–1017, https://doi.org/10.1016/j.promfg.2016.08.089.

[15] P. Krakhmalev, I. Yadroitsava, G. Fredriksson, I. Yadroitsev, In situ heat treatment in selective laser melted martensitic AISI 420 stainless steels, Mater. Des. 87 (2015) 380–385, https://doi.org/10.1016/j.matdes.2015.08.045.

[16] N. Haghdadi, E. Whitelock, B. Lim, H. Chen, X. Liao, S.S. Babu, S.P. Ringer, S. Primig, Multimodal γ' precipitation in Inconel-738 Ni-based superalloy during electron-beam powder bed fusion additive manufacturing, J. Mater. Sci. 55 (2020) 13342–13350, https://doi.org/10.1007/s10853-020-04915-w.

[17] B. Lim, H. Chen, Z. Chen, N. Haghdadi, X. Liao, S. Primig, S.S. Babu, A. Breen, S. P. Ringer, Microstructure–property gradients in Ni-based superalloy (Inconel 738) additively manufactured via electron beam powder bed fusion, Addit. Manuf. (2021), 102121, https://doi.org/10.1016/j.addma.2021.102121.

[18] P. Karimi, E. Sadeghi, P. Åkerfeldt, J. Ålgårdh, J. Andersson, Influence of successive thermal cycling on microstructure evolution of EBM-manufactured alloy 718 in track-by-track and layer-by-layer design, Mater. Des. 160 (2018) 427–441, https://doi.org/10.1016/j.matdes.2018.09.038.

[19] E. Chauvet, P. Kontis, E.A. Jägle, B. Gault, D. Raabe, C. Tassin, J.J. Blandin, R. Dendievel, B. Vayre, S. Abed, G. Martin, Hot cracking mechanism affecting a non-weldable Ni-based superalloy produced by selective electron Beam Melting, Acta Mater. 142 (2018) 82–94, https://doi.org/10.1016/j.actamat.2017.09.047.

[20] M. Ramsperger, R.F. Singer, C. Körner, Microstructure of the nickel-base superalloy CMSX-4 fabricated by selective electron beam melting, Metall. Mater. Trans. A Phys. Metall. Mater. Sci. 47 (2016) 1469–1480, https://doi.org/10.1007/s11661-015-3300-y.

[21] B. Zhang, P. Wang, Y. Chew, Y. Wen, M. Zhang, P. Wang, G. Bi, J. Wei, Mechanical properties and microstructure evolution of selective laser melting Inconel 718 along building direction and sectional dimension, Mater. Sci. Eng. A 794 (2020), 139941, https://doi.org/10.1016/j.msea.2020.139941.

[22] C. Körner, M. Ramsperger, C. Meid, D. Bürger, P. Wollgramm, M. Bartsch, G. Eggeler, Microstructure and mechanical properties of CMSX-4 single crystals prepared by additive manufacturing, Metall. Mater. Trans. A Phys. Metall. Mater. Sci. 49 (2018) 3781–3792, https://doi.org/10.1007/s11661-018-4762-5.

[23] B. Lim, H. Chen, K. Nomoto, Z. Chen, A.I. Saville, S. Vogel, A.J. Clarke, A. Paradowska, M. Reid, S. Primig, X. Liao, S.S. Babu, A.J. Breen, S.P. Ringer, Additively manufactured Haynes-282 monoliths containing thin wall struts of varying thicknesses, Addit. Manuf. 59 (2022), 103120, https://doi.org/10.1016/j.addma.2022.103120.

[24] C.L.A. Leung, S. Marussi, R.C. Atwood, M. Towrie, P.J. Withers, P.D. Lee, In situ X-ray imaging of defect and molten pool dynamics in laser additive manufacturing, Nat. Commun. 9 (2018) 1–9, https://doi.org/10.1038/s41467-018-03734-7.

[25] C. Zhao, K. Fezzaa, R.W. Cunningham, H. Wen, F. De Carlo, L. Chen, A.D. Rollett, T. Sun, Real-time monitoring of laser powder bed fusion process using high-speed X-ray imaging and diffraction, Sci. Rep. 7 (2017) 1–11, https://doi.org/10.1038/s41598-017-03761-2.

[26] C. Kenel, D. Grolimund, X. Li, E. Panepucci, V.A. Samson, D.F. Sanchez, F. Marone, C. Leinenbach, In situ investigation of phase transformations in Ti-6Al-4V under additive manufacturing conditions combining laser melting and high-speed micro-X-ray diffraction, Sci. Rep. 7 (2017) 1–10, https://doi.org/10.1038/s41598-017-16760-0.

[27] W.L. Bevilaqua, J. Epp, H. Meyer, J. Dong, H. Roelofs, A. da, S. Rocha, A. Reguly, Revealing the dynamic transformation of austenite to bainite during uniaxial warm compression through in-situ synchrotron X-ray diffraction, Metals 11 (2021) 1–14, https://doi.org/10.3390/met11030467.

[28] B. Wahlmann, E. Krohmer, C. Breuning, N. Schell, P. Staron, E. Uhlmann, C. Körner, In situ observation of γ' phase transformation dynamics during selective laser melting of CMSX-4, Adv. Eng. Mater. 23 (2021), https://doi.org/10.1002/adem.202100112.

[29] M. Shiomi, A. Yoshidome, F. Abe, K. Osakada, Finite element analysis of melting and solidifying processes in laser rapid prototyping of metallic powders, Int. J. Mach. Tools Manuf. 39 (1999) 237–252, https://doi.org/10.1016/S0890-6955(98)00036-4.

[30] A. Ilin, R. Logvinov, A. Kulikov, A. Prihodovsky, H. Xu, V. Ploshikhin, B. Günther, F. Bechmann, Computer aided optimisation of the thermal management during laser beam melting process, Phys. Procedia 56 (2014) 390–399, https://doi.org/10.1016/J.PHPRO.2014.08.142.

[31] R. Acharya, J.A. Sharon, A. Staroselsky, Prediction of microstructure in laser powder bed fusion process, Acta Mater. 124 (2017) 360–371, https://doi.org/10.1016/J.ACTAMAT.2016.11.018.

[32] H.L. Wei, J.W. Elmer, T. Debroy, Origin of grain orientation during solidification of an aluminum alloy, Acta Mater. 115 (2016) 123–131, https://doi.org/10.1016/J.ACTAMAT.2016.05.057.

[33] O. Zinovieva, A. Zinoviev, V. Ploshikhin, Three-dimensional modeling of the microstructure evolution during metal additive manufacturing, Comput. Mater. Sci. 141 (2018) 207–220, https://doi.org/10.1016/J.COMMATSCI.2017.09.018.

[34] M.J. Anderson, C. Panwisawas, Y. Sovani, R.P. Turner, J.W. Brooks, H. C. Basoalto, Mean-field modelling of the intermetallic precipitate phases during heat treatment and additive manufacture of Inconel 718, Acta Mater. 156 (2018) 432–445, https://doi.org/10.1016/J.ACTAMAT.2018.07.002.

[35] M.J. Anderson, J. Benson, J.W. Brooks, B. Saunders, H.C. Basoalto, Predicting precipitation kinetics during the annealing of additive manufactured Inconel 625 components, Integr. Mater. Manuf. Innov. 8 (2019) 154–166, https://doi.org/10.1007/S40192-019-00134-7/FIGURES/11.

[36] H.C. Basoalto, C. Panwisawas, Y. Sovani, M.J. Anderson, R.P. Turner, B. Saunders, J.W. Brooks, A computational study on the three-dimensional printability of precipitate-strengthened nickel-based superalloys, Proc. R. Soc. A 474 (2018), https://doi.org/10.1098/RSPA.2018.0295.

[37] K. McNamara, Y. Ji, F. Lia, P. Promoppatum, S.C. Yao, H. Zhou, Y. Wang, L. Q. Chen, R.P. Martukanitz, Predicting phase transformation kinetics during metal additive manufacturing using non-isothermal Johnson-Mehl-Avrami models: application to Inconel 718 and Ti-6Al-4V, Addit. Manuf. 49 (2022), 102478, https://doi.org/10.1016/J.ADDMA.2021.102478.

[38] R. Radis, M. Schaffer, M. Albu, G. Kothleitner, P. Pölt, E. Kozeschnik, Multimodal size distributions of γ' precipitates during continuous cooling of UDIMET 720 Li, Acta Mater. 57 (2009) 5739–5747, https://doi.org/10.1016/j.actamat.2009.08.002.

[39] A. Drexler, B. Oberwinkler, S. Primig, C. Turk, E. Povoden-karadeniz, A. Heinemann, W. Ecker, M. Stockinger, Materials Science & Engineering A Experimental and numerical investigations of the γ'' and γ' precipitation kinetics in Alloy 718, Mater. Sci. Eng. A. 723 (2018) 314–323, https://doi.org/10.1016/j.msea.2018.03.013.

[40] M. Pudar, S. Zamberger, K. Spiradek-Hahn, R. Radis, E. Kozeschnik, Computational analysis of precipitation during continuous casting of microalloyed steel, Steel Res. Int. 81 (2010) 372–380, https://doi.org/10.1002/SRIN.201000021.

[41] M. Werinos, H. Antrekowitsch, E. Kozeschnik, T. Ebner, F. Moszner, J.F. Löffler, P.J. Uggowitzer, S. Pogatscher, Ultrafast artificial aging of Al–Mg–Si alloys, Scr. Mater. 112 (2016) 148–151, https://doi.org/10.1016/J.SCRIPTAMAT.2015.09.037.

[42] J. Svoboda, F.D. Fischer, P. Fratzl, E. Kozeschnik, Modelling of kinetics in multi-component multi-phase systems with spherical precipitates I: theory, Mater. Sci. Eng. A 385 (2004) 166–174, https://doi.org/10.1016/j.msea.2004.06.018.

[43] B. Stump, A. Plotkowski, An adaptive integration scheme for heat conduction in additive manufacturing, Appl. Math. Model. 75 (2019) 787–805, https://doi.org/10.1016/j.apm.2019.07.008.

[44] A.V. Sotov, A.V. Agapovichev, V.G. Smelov, V.V. Kokareva, M.O. Dmitrieva, A. A. Melnikov, S.P. Golanov, Y.M. Anurov, Investigation of the IN-738 superalloy microstructure and mechanical properties for the manufacturing of gas turbine engine nozzle guide vane by selective laser melting, Int. J. Adv. Manuf. Technol. 107 (2020) 2525–2535, https://doi.org/10.1007/s00170-020-05197-x.

[45] F. Theska, A. Stanojevic, B. Oberwinkler, S.P. Ringer, S. Primig, On conventional versus direct ageing of Alloy 718, Acta Mater. 156 (2018) 116–124, https://doi.org/10.1016/j.actamat.2018.06.034.

[46] T.M. Pollock, S. Tin, Nickel-based superalloys for advanced turbine engines: chemistry, microstructure, and properties, J. Propuls. Power 22 (2006) 361–374, https://doi.org/10.2514/1.18239.

[47] O.A. Ojo, N.L. Richards, M.C. Chaturvedi, On incipient melting during high temperature heat treatment of cast Inconel 738 superalloy, J. Mater. Sci. 39 (2004) 7401–7404, https://doi.org/10.1023/B:JMSC.0000048761.32712.eb.

[48] A.T. Egbewande, R.A. Buckson, O.A. Ojo, Analysis of laser beam weldability of Inconel 738 superalloy, Mater. Charact. 61 (2010) 569–574, https://doi.org/10.1016/j.matchar.2010.02.016.

[49] S. Sanchez, P. Smith, Z. Xu, G. Gaspard, C.J. Hyde, W.W. Wits, I.A. Ashcroft, H. Chen, A.T. Clare, Powder Bed Fusion of nickel-based superalloys: a review, Int. J. Mach. Tools Manuf. 165 (2021), https://doi.org/10.1016/j.ijmachtools.2021.103729.

[50] C.L.A. Leung, R. Tosi, E. Muzangaza, S. Nonni, P.J. Withers, P.D. Lee, Effect of preheating on the thermal, microstructural and mechanical properties of selective electron beam melted Ti-6Al-4V components, Mater. Des. 174 (2019), 107792, https://doi.org/10.1016/j.matdes.2019.107792.

[51] S. Griffiths, H. Ghasemi Tabasi, T. Ivas, X. Maeder, A. De Luca, K. Zweiacker, R. Wróbel, J. Jhabvala, R.E. Logé, C. Leinenbach, Combining alloy and process modification for micro-crack mitigation in an additively manufactured Ni-base superalloy, Addit. Manuf. 36 (2020), https://doi.org/10.1016/j.addma.2020.101443.

[52] P. Soille, L. Vincent Pierre Soille, L.M. Vincent, Determining watersheds in digital pictures via flooding simulations, Https://Doi.Org/10.1117/12.24211. 1360 (1990) 240–250. https://doi.org/10.1117/12.24211.

[53] ASTM Standard Test Method for Microindentation Hardness of MaterialsKnoop and Vickers Hardness of Materials 1, Annu. B ASTM Stand. i 2010 1 42.

[54] K.C. Russell, Nucleation in solids: the induction and steady state effects, Adv. Colloid Interface Sci. 13 (1980) 205–318, https://doi.org/10.1016/0001-8686(80)80003-0.

[55] K. Janssens, D. Raabe, E. Kozeschnik, M. Miodownik, B. Nestler, Computational Materials Engineering, first ed., Elsevier, 2007 https://doi.org/10.1016/B978-0-12-369468-3.X5000-X.

[56] B. Sonderegger, E. Kozeschnik, Generalized nearest-neighbor broken-bond analysis of randomly oriented coherent interfaces in multicomponent Fcc and Bcc structures, Metall. Mater. Trans. A Phys. Metall. Mater. Sci. 40 (2009) 499–510, https://doi.org/10.1007/S11661-008-9752-6/FIGURES/8.

[57] B. Sonderegger, E. Kozeschnik, Size dependence of the interfacial energy in the generalized nearest-neighbor broken-bond approach, Scr. Mater. 60 (2009) 635–638, https://doi.org/10.1016/J.SCRIPTAMAT.2008.12.025.

[58] B. Sonderegger, E. Kozeschnik, Interfacial energy of diffuse phase boundaries in the generalized broken-bond approach, Metall. Mater. Trans. A Phys. Metall.

Mater. Sci. 41 (2010) 3262–3269, https://doi.org/10.1007/S11661-010-0370-8/FIGURES/4.
[59] E. Kozeschnik, J. Svoboda, F.D. Fischer, Modified evolution equations for the precipitation kinetics of complex phases in multi-component systems 28 (2005) 379–382, https://doi.org/10.1016/j.calphad.2004.11.003.
[60] R. Kampmann, R. Wagner, KInetics of precipitation in metastable binary alloys -theory and application to Cu-1.9 at% Ti AND Ni-14 at% Al, in: Decompos. Alloy. Early Stages, Elsevier, 1984, pp. 91–103, https://doi.org/10.1016/B978-0-08-031651-2.50018-5.
[61] E. Kozeschnik, J. Svoboda, P. Fratzl, F.D. Fischer, Modelling of kinetics in multi-component multi-phase systems with spherical precipitates II: numerical solution and application, Mater. Sci. Eng. A 385 (2004) 157–165, https://doi.org/10.1016/j.msea.2004.06.016.
[62] J. Risse, Additive Manufacturing of Nickel-Base Superalloy IN738LC by Laser Powder Bed Fusion, (2019).
[63] F.L. Reyes Tirado, D.C. Dunand, Increasing γ' volume fraction in Co–Nb–V- and Co–Ta–V-based superalloys, J. Mater. Res. Technol. 11 (2021) 2305–2313, https://doi.org/10.1016/J.JMRT.2021.02.028.
[64] E. Kozeschnik, Modeling Solid-State Precipitation, Momentum Press, 2012, https://doi.org/10.5643/9781606500644.
[65] B. Wahlmann, F. Galgon, A. Stark, S. Gayer, N. Schell, P. Staron, C. Körner, Growth and coarsening kinetics of gamma prime precipitates in CMSX-4 under simulated additive manufacturing conditions, Acta Mater. 180 (2019) 84–96, https://doi.org/10.1016/j.actamat.2019.08.049.
[66] M. Avrami, Granulation, phase change, and microstructure kinetics of phase change. III, J. Chem. Phys. 9 (1941) 177–184, https://doi.org/10.1063/1.1750872.
[67] P. Strunz, M. Petrenec, J. Polák, U. Gasser, G. Farkas, Formation and dissolution of' precipitates in IN792 superalloy at elevated temperatures, Metals 6 (2016), https://doi.org/10.3390/met6020037.
[68] A.R.P. Singh, S. Nag, J.Y. Hwang, G.B. Viswanathan, J. Tiley, R. Srinivasan, H. L. Fraser, R. Banerjee, Influence of cooling rate on the development of multiple generations of γ' precipitates in a commercial nickel base superalloy, Mater. Charact. 62 (2011) 878–886, https://doi.org/10.1016/j.matchar.2011.06.002.
[69] E. Balikci, A. Raman, R. Mirshams, Microstructure evolution in polycrystalline IN738LC in the range 1120 to 1250C, Zeitschrift Fuer, Met 90 (1999) 132–140.
[70] E. Balikci, D. Erdeniz, Multimodal precipitation in the superalloy IN738LC, Metall. Mater. Trans. A Phys. Metall. Mater. Sci. 41 (2010) 1391–1398, https://doi.org/10.1007/s11661-010-0241-3.
[71] Ł. Rakoczy, M. Grudzień-Rakoczy, F. Hanning, G. Cempura, R. Cygan, J. Andersson, A. Zielińska-Lipiec, Investigation of the γ' precipitates dissolution in a Ni-based superalloy during stress-free short-term annealing at high homologous temperatures, Metall. Mater. Trans. A Phys. Metall. Mater. Sci. 52 (2021) 4767–4784, https://doi.org/10.1007/s11661-021-06420-4.
[72] E. Balikci, A. Raman, Characteristics of the γ' precipitates at high temperatures in Ni-base polycrystalline superalloy IN738LC, J. Mater. Sci. 35 (2000) 3593–3597, https://doi.org/10.1023/A:1004869714854.
[73] F. Masoumi, D. Shahriari, M. Jahazi, J. Cormier, A. Devaux, Kinetics and Mechanisms of γ' Reprecipitation in a Ni-based Superalloy, Sci. Rep. 6 (2016) 1–16, https://doi.org/10.1038/srep28650.
[74] A.R.P. Singh, S. Nag, S. Chattopadhyay, Y. Ren, J. Tiley, G.B. Viswanathan, H. L. Fraser, R. Banerjee, Mechanisms related to different generations of γ' precipitation during continuous cooling of a nickel base superalloy, Acta Mater. 61 (2013) 280–293, https://doi.org/10.1016/j.actamat.2012.09.058.
[75] O.M.D.M. Messé, R. Muñoz-Moreno, T. Illston, S. Baker, H.J. Stone, Metastable carbides and their impact on recrystallisation in IN738LC processed by selective laser melting, Addit. Manuf. 22 (2018) 394–404, https://doi.org/10.1016/j.addma.2018.05.030.
[76] N.D. Souza, M.C. Hardy, B. Roebuck, W.E.I. Li, G.D. West, D.M. Collins, On the Rate Dependence of Precipitate Formation and Dissolution in a Nickel-Base Superalloy, Metall. Mater. Trans. A. (n.d.). https://doi.org/10.1007/s11661–022-06680–8.
[77] M. Jahazi, A.R. Mashreghi, Dissolution and precipitation kinetics of γ' in nickel base superalloy Udimet 520, Mater. Sci. Technol. 18 (2002) 458–462, https://doi.org/10.1179/026708302225001606.
[78] H. Huang, G. Liu, H. Wang, A. Ullah, B. Hu, Dissolution behavior and kinetics of γ' phase during solution treatment in powder metallurgy nickel-based superalloy, Metall. Mater. Trans. A. 51 (2020) 1075–1084, https://doi.org/10.1007/s11661-019-05581-7.
[79] H. Huang, G. Liu, H. Wang, A. Ullah, B. Hu, Dissolution behavior and kinetics of γ' phase during solution treatment in powder metallurgy nickel-based superalloy, Metall. Mater. Trans. A Phys. Metall. Mater. Sci. 51 (2020) 1075–1084, https://doi.org/10.1007/s11661-019-05581-7.
[80] A.J. Goodfellow, E.I. Galindo-Nava, K.A. Christofidou, N.G. Jones, T. Martin, P.A. J. Bagot, C.D. Boyer, M.C. Hardy, H.J. Stone, Gamma prime precipitate evolution during aging of a model nickel-based superalloy, Metall. Mater. Trans. A Phys. Metall. Mater. Sci. 49 (2018) 718–728, https://doi.org/10.1007/s11661-017-4336-y.
[81] T.P. Gabb, D.G. Backman, D.Y. Wei, D.P. Mourer, D. Furrer, A. Garg, D.L. Ellis, #947;' Form. a Nickel-Base Disk Superalloy 2012 405 414 doi: 10.7449/2000/superalloys_2000_405_414.
[82] A. Plati, Modelling of γ precipitation in superalloys University of Cambridge, Mater. Sci. (2003) 73.
[83] V.V. Rielli, F. Theska, F. Godor, A. Stanojevic, B. Oberwinkler, S. Primig, Evolution of nanoscale precipitates during common Alloy 718 ageing treatments, Mater. Des. 205 (2021), 109762, https://doi.org/10.1016/j.matdes.2021.109762.
[84] T. Grosdidier, A. Hazotte, A. Simon, Precipitation and dissolution processes in γ/γ' single crystal nickel-based superalloys, Mater. Sci. Eng. A. 256 (1998) 183–196, https://doi.org/10.1016/s0921-5093(98)00795-3.
[85] E. Balikci, A. Raman, R.A. Mirshams, Influence of various heat treatments on the microstructure of polycrystalline IN738LC, Metall. Mater. Trans. A Phys. Metall. Mater. Sci. 28 (1997) 1993–2003, https://doi.org/10.1007/s11661-997-0156-9.
[86] K. Thornton, N. Akaiwa, P.W. Voorhees, Large-scale simulations of Ostwald ripening in elastically stressed solids: I. Development of microstructure, Acta Mater. 52 (2004) 1353–1364, https://doi.org/10.1016/j.actamat.2003.11.037.
[87] S. Tang, L.K. Ning, T.Z. Xin, Z. Zheng, Coarsening behavior of gamma prime precipitates in a nickel based single crystal superalloy, J. Mater. Sci. Technol. 32 (2016) 172–176, https://doi.org/10.1016/j.jmst.2015.10.005.
[88] S.S. Babu, M.K. Miller, J.M. Vitek, S.A. David, Characterization of the microstructure evolution in a nickel base superalloy during continuous cooling conditions, Acta Mater. 49 (2001) 4149–4160, https://doi.org/10.1016/S1359-6454(01)00314-7.
[89] M. Zhang, G.Q. Liu, H. Wang, B.F. Hu, Stability of γ' multimodal microstructure in a Ni-based powder metallurgy superalloy, Sci. China Technol. Sci. 61 (2018) 1824–1828, https://doi.org/10.1007/s11431-018-9372-8.
[90] P.M. Sarosi, B. Wang, J.P. Simmons, Y. Wang, M.J. Mills, Formation of multimodal size distributions of γ' in a nickel-base superalloy during interrupted continuous cooling, Scr. Mater. 57 (2007) 767–770, https://doi.org/10.1016/j.scriptamat.2007.06.014.
[91] F. Theska, W.F. Tse, B. Schulz, R. Buerstmayr, S.R. Street, M. Lison-Pick, S. Primig, Review of microstructure–mechanical property relationships in cast and wrought ni-based superalloys with boron, carbon, and zirconium microalloying additions, Adv. Eng. Mater. (2022) 2201514, https://doi.org/10.1002/ADEM.202201514.
[92] Y. Li, X. Liang, G. Peng, F. Lin, Effect of heat treatments on the microstructure and mechanical properties of IN738LC prepared by electron beam powder bed fusion, J. Alloy. Compd. 918 (2022), 165807, https://doi.org/10.1016/j.jallcom.2022.165807.
[93] L. Zhang, Y. Li, Q. Zhang, S. Zhang, Microstructure evolution, phase transformation and mechanical properties of IN738 superalloy fabricated by selective laser melting under different heat treatments, Mater. Sci. Eng. A 844 (2022), 142947, https://doi.org/10.1016/j.msea.2022.142947.
[94] J.C. Franco-Correa, E. Martínez-Franco, J.M. Alvarado-Orozco, L.A. Cáceres-Díaz, D.G. Espinosa-Arbelaez, J.A. Villada, Effect of conventional heat treatments on the microstructure and microhardness of IN718 obtained by wrought and additive manufacturing, J. Mater. Eng. Perform. 30 (2021) 7035–7045, https://doi.org/10.1007/s11665-021-06138-9.
[95] N. El-Bagoury, M. Waly, A. Nofal, Effect of various heat treatment conditions on microstructure of cast polycrystalline IN738LC alloy, Mater. Sci. Eng. A 487 (2008) 152–161, https://doi.org/10.1016/J.MSEA.2007.10.004.
[96] N. Li, M.J. Anderson, H.C. Basoalto, Automated stereology and uncertainty quantification considering spherical non-penetrating dispersions, Page 464. Cryst 2023 Vol. 13 (13) (2023) 464, https://doi.org/10.3390/CRYST13030464.
[97] W.T. Loomis, J.W. Freeman, D.L. Sponseller, Influence of molybdenum on the γ'-phase in experimental nickelbase superalloys, Met. Trans. 3 (1972) 989–1000.
[98] A.S. Shaikh Development of a γ' Precipitation Hardening Ni-Base Superalloy for Additive Manufacturing Thesis 2018 102.⟨https://odr.chalmers.se/handle/20.500.12380/255645%0Ahttps://www.researchgate.net/profile/Abdul_Shaafi_Shaikh2/publication/326226200%0Ahttps://drive.google.com/open?id=1BIez-aJyBTjnSgazzzTvv3jlrYpFC0N-⟩.
[99] P. Caron High. γ' Solvus N. Gener. Nickel-Based Superalloys Single Cryst. Turbine Bl. Appl. 5 2000 737 746 doi: 10.7449/2000/superalloys_2000_737_746.
[100] R. Rosenthal, D.R.F. West, Continuous γ' precipitation in directionally solidified IN738 LC alloy, Mater. Sci. Technol. 15 (1999) 1387–1394, https://doi.org/10.1179/026708399101505518.
[101] P. Michaleris, Modeling metal deposition in heat transfer analyses of additive manufacturing processes, Finite Elem. Anal. Des. 86 (2014) 51–60, https://doi.org/10.1016/J.FINEL.2014.04.003.
[102] P.N. Quested, R.F. Brooks, L. Chapman, R. Morrell, Y. Youssef, K.C. Mills, Measurement and estimation of thermophysical properties of nickel based superalloys, Mater. Sci. Technol. 25 (2009) 154–162, https://doi.org/10.1179/174328408×361454.
[103] D. Deng, J. Moverare, R.L. Peng, H. Söderberg, Microstructure and anisotropic mechanical properties of EBM manufactured Inconel 718 and effects of post heat treatments, Mater. Sci. Eng. A 693 (2017) 151–163, https://doi.org/10.1016/j.msea.2017.03.085.
[104] D. Deng, R.L. Peng, H. Söderberg, J. Moverare, On the formation of microstructural gradients in a nickel-base superalloy during electron beam melting, Mater. Des. 160 (2018) 251–261, https://doi.org/10.1016/j.matdes.2018.09.006.
[105] B.S. Bokstein, S.Z. Bokstein, I.T. Spitsberg, Ni self-diffusion in alloyed Ni3Al, Intermetallics 4 (1996) 517–523, https://doi.org/10.1016/0966-9795(96)00038-6.
[106] J. Cermak, V. Rothova, Concentration dependence of ternary interdiffusion coefficients in Ni3Al/Ni3Al-X couples with X = Cr, Fe, Nb and Ti, Acta Mater. 51 (2003) 4411–4421, https://doi.org/10.1016/S1359-6454(03)00276-3.
[107] M. Li, J. Coakley, D. Isheim, G. Tian, B. Shollock, Influence of the initial cooling rate from γ' supersolvus temperatures on microstructure and phase compositions

in a nickel superalloy, J. Alloy. Compd. 732 (2018) 765–776, https://doi.org/10.1016/j.jallcom.2017.10.263.
[108] Y.Q. Chen, T.J.A. Slater, E.A. Lewis, E.M. Francis, M.G. Burke, M. Preuss, S. J. Haigh, Measurement of size-dependent composition variations for gamma prime (γ') precipitates in an advanced nickel-based superalloy, Ultramicroscopy 144 (2014) 1–8, https://doi.org/10.1016/j.ultramic.2014.04.001.
[109] Y.Q. Chen, E. Francis, J. Robson, M. Preuss, S.J. Haigh, Compositional variations for small-scale gamma prime (γ′) precipitates formed at different cooling rates in an advanced Ni-based superalloy, Acta Mater. 85 (2015) 199–206, https://doi.org/10.1016/j.actamat.2014.11.009.